nature cell biology

Matrix geometry determines optimal cancer cell migration strategy and modulates response to interventions

Melda Tozluoğlu[1], Alexander L. Tournier[1], Robert P. Jenkins[2], Steven Hooper[2], Paul A. Bates[1,3] and Erik Sahai[2,3]

The molecular requirements and morphology of migrating cells can vary depending on matrix geometry; therefore, predicting the optimal migration strategy or the effect of experimental perturbation is difficult. We present a model of cell motility that encompasses actin-polymerization-based protrusions, actomyosin contractility, variable actin–plasma membrane linkage leading to membrane blebbing, cell–extracellular-matrix adhesion and varying extracellular matrix geometries. This is used to explore the theoretical requirements for rapid migration in different matrix geometries. Confined matrix geometries cause profound shifts in the relationship of adhesion and contractility to cell velocity; indeed, cell–matrix adhesion is dispensable for migration in discontinuous confined environments. The model is challenged to predict the effect of different combinations of kinase inhibitors and integrin depletion *in vivo*, and in confined matrices based on *in vitro* two-dimensional measurements. Intravital imaging is used to verify bleb-driven migration at tumour margins, and the predicted response to single and combinatorial manipulations.

Cell migration depends on the interplay of actin polymerization, deformation of the plasma membrane, actomyosin contractility and cell–matrix adhesion. Cancer cells use different migratory strategies to invade into tissue[1,2], which represents a significant clinical problem. Further, the mode of cell migration determines the sensitivity of invading cancer cells to interventions that target either regulators of actin polymerization or actomyosin contractility[2–4]. This is a problem when attempting to extrapolate findings from simple *in vitro* experiments to the complex matrix environments that surround tumours.

Elongated, or mesenchymal, modes of migration rely on actin polymerization to push the plasma membrane forward. Amoeboid, or rounded, migration is highly dependent on actomyosin contractility[3]. However, the mechanical aspects of amoeboid migration modes are poorly understood. Hydrostatic pressure generated by actomyosin contractility may play a role. In this model, pressure causes the plasma membrane to detach from the actin cortex, leading to the formation of a bleb[5]. Although blebbing has been observed in many systems[6–11], the relation of blebs to migration is controversial. Blebs might simply be a consequence of high levels of contractility that do not aid motility. Further, different studies have reported blebs at the front, sides or rear of invading cancer cells[9,10,12].

Recent work has questioned the role of adhesion during migration in complex geometries. Depletion of all integrins does not impede the movement of dendritic cells in three-dimensional (3D) matrices[13]. Although the data are unequivocal, the interpretation is unclear and compensatory adhesion mechanisms cannot be excluded. Existing studies have modelled actin-polymerization-driven cell migration, but little attention has been paid to adhesion-free motility[14–16], and models of single membrane bleb initiation have not been related to cell migration[17,18]. Thus, at present, there is no unified framework to understand the interplay between complex matrix geometries and the forces generated by the cytoskeleton, hydrostatic pressure, membrane tension and matrix adhesion.

Here we describe a computational model that allows multiple cell migration factors to be investigated in different matrix geometries. This model predicts unexpected effects of matrix geometry on the relationship between adhesion, contractility and cell velocity. Adhesion-independent modes of migration are predicted in confined but discontinuous environments. In addition, the introduction of membrane blebbing changes the relationship between contractility and cell speed. The model is then used to predict the effect of numerous experimental perturbations on cell migration in different matrix geometries. Finally, we test the predictions by using a combination of *in vitro* experiments and intravital imaging of tumours.

[1]Biomolecular Modelling Laboratory, Cancer Research UK London Research Institute, 44 Lincoln's Inn Fields, London WC2A 3LY, UK. [2]Tumour Cell Biology Laboratory, Cancer Research UK London Research Institute, 44 Lincoln's Inn Fields, London WC2A 3LY, UK.
[3]Correspondence should be addressed to P.A.B. or E.S. (e-mail: paul.bates@cancer.org.uk or erik.sahai@cancer.org.uk)

Received 7 February 2013; accepted 1 May 2013; published online 23 June 2013; DOI: 10.1038/ncb2775

RESULTS

Generation of the cell migration model

We constructed a hybrid agent-based/finite-element model of cancer cell motility. The model cell has an actomyosin cortex interacting with an outer cell membrane. Both are represented as a set of agents (points) linked with viscoelastic elements (Fig. 1), and these elements have resistance to stretching, compression and bending. Local levels of actin cortex density, myosin concentration and cortex–membrane linker proteins are recorded at each agent. Local heterogeneity and temporal dynamics of these proteins influence the local physical properties of the cell as well as bleb and protrusion dynamics (Supplementary Note). Initiation of actin-polymerization-based protrusions is probabilistic. At protrusion tips, the membrane is pushed out with a constant force, mimicking polymerizing actin. F-actin-based protrusions can spread on matrix filaments and this increases their stability (Supplementary Note—Actin-polymerization-based protrusions). The internal cell body is modelled as a viscoelastic medium, with an ideal volume and resting pressure (Supplementary Note—Internal cell body). A bleb is initiated where the forces due to the internal pressure of the cell exceed the linker forces in accordance with the local level of cortex–membrane linker proteins, and the membrane detaches from the cortex (Supplementary Note—Blebs). This is followed by new actin polymerization on the detached membrane and depolymerization of the F-actin that is not attached to plasma membrane. This sequence of events typically leads to rapid bleb expansion, a period of stabilization associated with actin polymerization, and frequently retraction of the bleb back to the cell body. The cell is able to form local attachments to the extracellular matrix (ECM) filaments. Forces from the actomyosin cortex can act on the ECM; as the force exerted increases, the cell–ECM adhesions have a force-dependent probability of rupture (Supplementary Note—Cell–ECM interactions). Model construction theory and methodology are described in Supplementary Note.

Model parameterization

To parameterize the model, A375P melanoma cells were analysed *in vitro*. Attention was given to the relationship of contractile myosin activity with formation of F-actin protrusions and formation of membrane blebs (Supplementary Fig. S2A–D). Bleb sizes, expansion and retraction velocities were measured (Fig. 2b or Supplementary Fig. S1A–C), as well as F-actin re-accumulation in blebs, cortex–membrane linker distribution and available excess membrane (Supplementary Fig. S1D–K). A complete summary of all parameters used in the model is given in Supplementary Table S1. Parameters that could not be obtained from the literature nor measured directly were fitted to the experimental data (Fig. 2 and Supplementary Figs S1,S2); the fitting procedure is detailed in Supplementary Note—Experimental data fitting.

We next examined the emergent behaviour of the model. Placed on a surface, a serum-starved model cell spreads (Fig. 2c and Supplementary Fig S1L). When myosin activity is increased by twofold in the model (as occurs following 1% serum stimulation; Supplementary Fig. S2B), the spread surface decreases and membrane blebbing is observed (Supplementary Video S1 and Fig. 2c). This is in good agreement with the behaviour of A375P cells stimulated with 1% serum (Fig. 2d and Supplementary Video S2). Blebbing is strongly correlated with the overall myosin levels. Notably, the transition to blebbing shows a threshold behaviour both in the model and experimentally (Supplementary Fig. S1M).

Cell migration can be guided by graded environmental cues that induce asymmetries in cytoskeletal properties, and thereby promote directed cell behaviour[15,19,20]. We therefore introduced asymmetry into the model to mimic graded environmental cues. Spatial biases were introduced in the F-actin protrusion initiation probability or the contractile myosin function. To account for the stochastic nature of protrusion initiation, termination and local variations in cortex–membrane linkage, multiple simulations were run for each set of parameters. Asymmetrically increasing F-actin protrusion probability in the model leads to migration in the direction of protrusions (Fig. 3a). Increasing myosin function on one side of the cell leads to migration in the opposite direction. Implementing both asymmetries simultaneously led to increased velocity. For subsequent simulations we linked increasing F-actin protrusion probability inversely with contractile myosin function; this was done both at the cellular and local level. The nature of the inverse function was determined from experimental measurements of the relationship between these two parameters (Supplementary Fig. S2D). These observations confirm that cell protrusion at the front and contractility at the rear cooperate during cell migration.

Matrix geometry determines optimal migration strategy

We next sought to understand the levels and distribution of parameters that confer the maximum velocity in different matrix geometries. To explore this relationship, we constructed three matrix geometries that represented a planar surface, a confined but continuous environment (analogous to a movement in a tube or between tissue planes), and a confined but discontinuous environment (analogous to traversing a network of fibres; Fig. 3b). For each of these matrix geometries we explored varying combinations of the following parameters: F-actin protrusion probability, contractile force, cortex–membrane interaction strength and cell–matrix adhesion.

For continuous surfaces, simulations show the highest cell velocity at intermediate levels of cell–ECM adhesion (Fig. 3b, surface data). Increasing adhesion values increased the amount of myosin function required for optimal migration speeds (Fig. 3b, surface). At low levels of adhesion, high levels of contractility reduced cell speed because high contractility is linked to reduced F-actin-polymerization-driven protrusions (Supplementary Fig. S2d), and high contractility also led to cell detachment. For non-confined surfaces, cells with F-actin protrusions showed the highest velocities. Forces exerted on the matrix were non-uniformly distributed along the length of the cell–matrix interface. Relatively high forces parallel to the matrix were exerted in a zone slightly behind the protrusion and forces with a large component perpendicular to the ECM were present at the cell rear (Fig. 3c(i)). These forces cause the detachment of the cell rear in the model (Supplementary Video S3). Blebbing-based strategies do not perform well on non-confined continuous surfaces (Fig. 3b).

A confined environment modifies the contractility–velocity relationship

To simulate a confined environment, we employed two continuous surfaces with the cell sandwiched between them. This predicted two different strategies with high velocity: at moderate levels of contractility, protrusions alone are the most effective strategy and relatively large

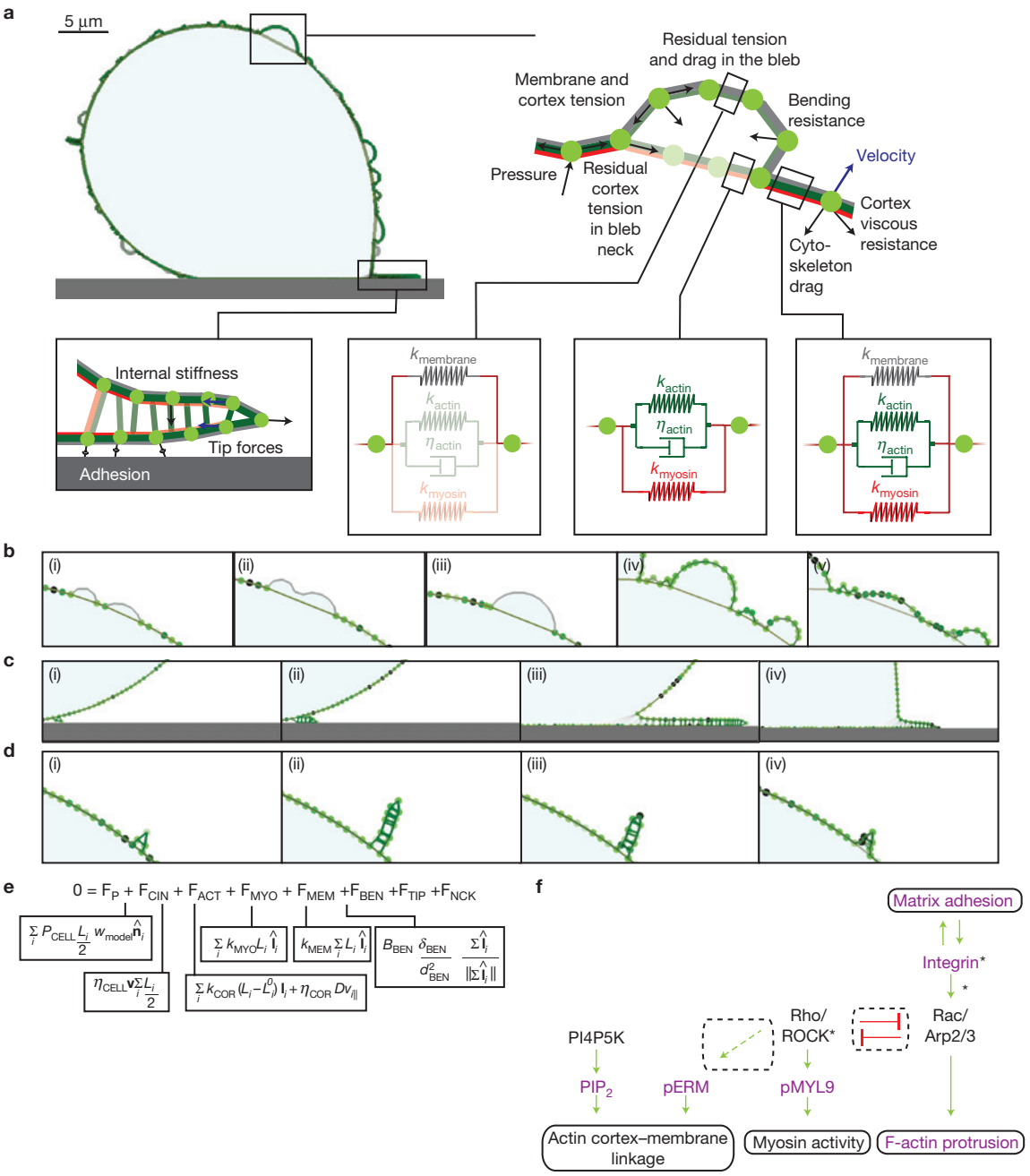

Figure 1 A hybrid agent-based/finite-element model of the cell. (**a**) The model cell is composed of a set of agents linked by viscoelastic elements. Scale bar, 5 μm. The linkers between the agents define the viscoelastic actin cortex with a Kelvin–Voigt body (green); tensions from myosin (red) and membrane (grey) are modelled as springs. Blebbing regions of the cell surface have greatly reduced actin cortex strength and initially no myosin. Bleb necks have a separate layer of cortex that depolymerizes. Forces acting on agents are shown. Actin protrusions elongate with the polymerization force acting on the protrusion tip. Newly polymerized actin does not have myosin; myosin diffuses inside the protrusion from the cytosol. Cell–ECM adhesion strength is dependent on the concentration of adhesion proteins on the cell surface. See also Supplementary Fig. S1. (**b**) Model snapshots showing lifetime of blebs. (i) Initiation of two blebs, with low actin and no myosin at the bleb rim. (ii, iii) During expansion, tearing of the blebbing membrane from the cortex on the sides merges the two blebs. (iv) Stabilization starts with actin accumulation at the bleb rim. (v) Retraction of the bleb. (**c**) An actin protrusion spreading on a surface. (i) Initiation of the protrusion. (ii, iii) The protrusion hits the ECM surface and starts spreading. (iv) Spreading of the cell body following the protrusion, and retraction of the protrusion. (**d**) An actin protrusion elongating away from any ECM surface. (i) Initiation. (ii) Reaching the thermodynamic limit for unsupported elongation. (iii, iv) Retraction. (**b**–**d**) The colour of the linkers represent actin density (green), myosin concentration (red) and membrane (light grey). The colour intensities scaled to protein concentrations are overlaid, generating the colour orange for high myosin–high actin regions. Cortex–membrane linker density is represented on agents; the darker the green, the higher the concentration. (**e**) The system is over-damped; velocities are calculated such that the forces acting on each agent are balanced by the viscous drag from the cortex and the cytosol. (**f**) Major molecular players and connections involved in the regulation of cortex–membrane linkage, F-actin protrusion, myosin activity and matrix adhesion are shown. Ovals, parameters in the model; dashed ovals, relationships between parameters that we explored computationally; purple text, variables that were measured; asterisks, points of experimental perturbation.

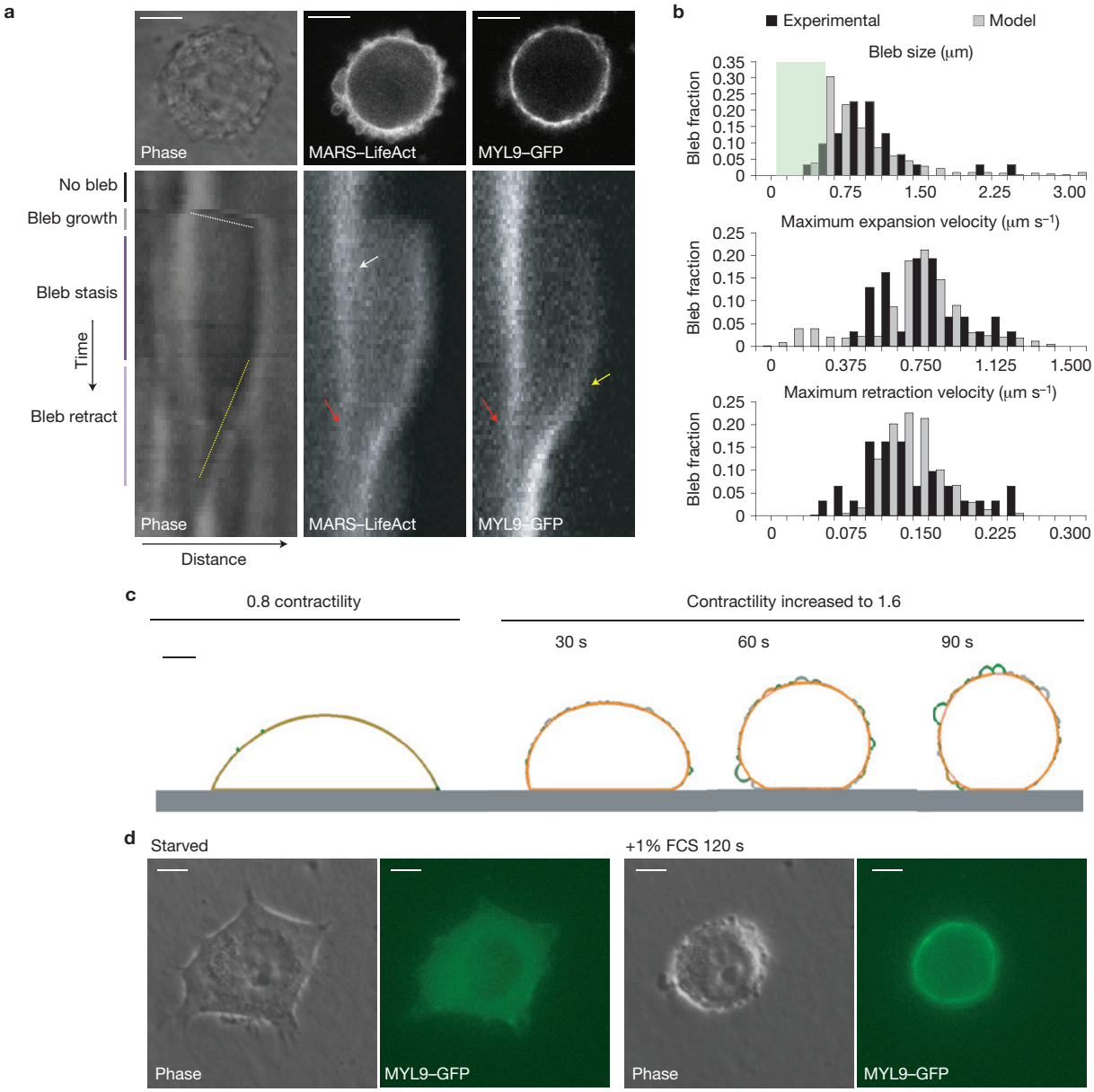

Figure 2 Comparison of experimental and model blebbing. (**a**) Bleb kymographs. The time axis (*y*) spans 150 s and the distance axis (*x*) spans 5.5 μm. The rapid expansion (indicated with white line), stabilization and slower retraction (indicated with yellow line) can be seen. Increased F-actin levels are roughly coincident with stabilization of the bleb (white arrow) and increasing myosin light chain (MLC; known as MYL9) levels are coincident with retraction of the bleb (yellow arrow). The residual cortex at the neck of the bleb is indicated with a white arrow, and its decay with red arrows. Upper panels show snapshots of the time series from which the kymographs were generated. Scale bars, 10 μm. (**b**) Maximum sizes, maximum expansion and maximum retraction velocities of blebs. Experimental measurements (black) and model outputs (grey). Experiments were done at 1% serum stimulation and the model at equivalent actomyosin levels. Green shading in upper panel indicates the zone where the limits of optical microscopy impact the ability to make accurate measurements. See Supplementary Fig. S2 for electron microscopy analysis and further parameterization measurements. (**c**) Model cell allowed to spread on surface for 400 s, and stimulated to double its initial myosin levels. The contractility levels indicated on the figure are normalized to A375P cells used in parameterization. Snapshots 30, 60 and 90 s after serum stimulation are shown, see Supplementary Video S1. Scale bar, 5 μm. Cell membrane is represented in grey, actin cortex in green and myosin in red. (**d**) Left, serum-starved A375P cell. Right, 120 s after 1% serum stimulation where blebbing is observed. Scale bars, 5 μm.

forces are exerted on the matrix parallel to the direction of migration (Fig. 3c(ii) and Supplementary Video S4). At high levels of contractility blebbing becomes the most effective migration strategy. In this setting, smaller outward forces perpendicular to the direction of migration predominate (Fig. 3c(iii) and Supplementary Video S5). Bleb-driven migration produces a shift in the relationship between myosin contraction and cell velocity (Fig. 3b—middle column of matrices). In contrast to movement on an unconfined surface, increasing myosin function leads to increased cell velocity. This occurs over a large range of parameter space, encompassing blebbing-based and bleb- and protrusion-based strategies, and for all cell–matrix adhesion values above zero. The confined nature of the environment means that high contractility is unable

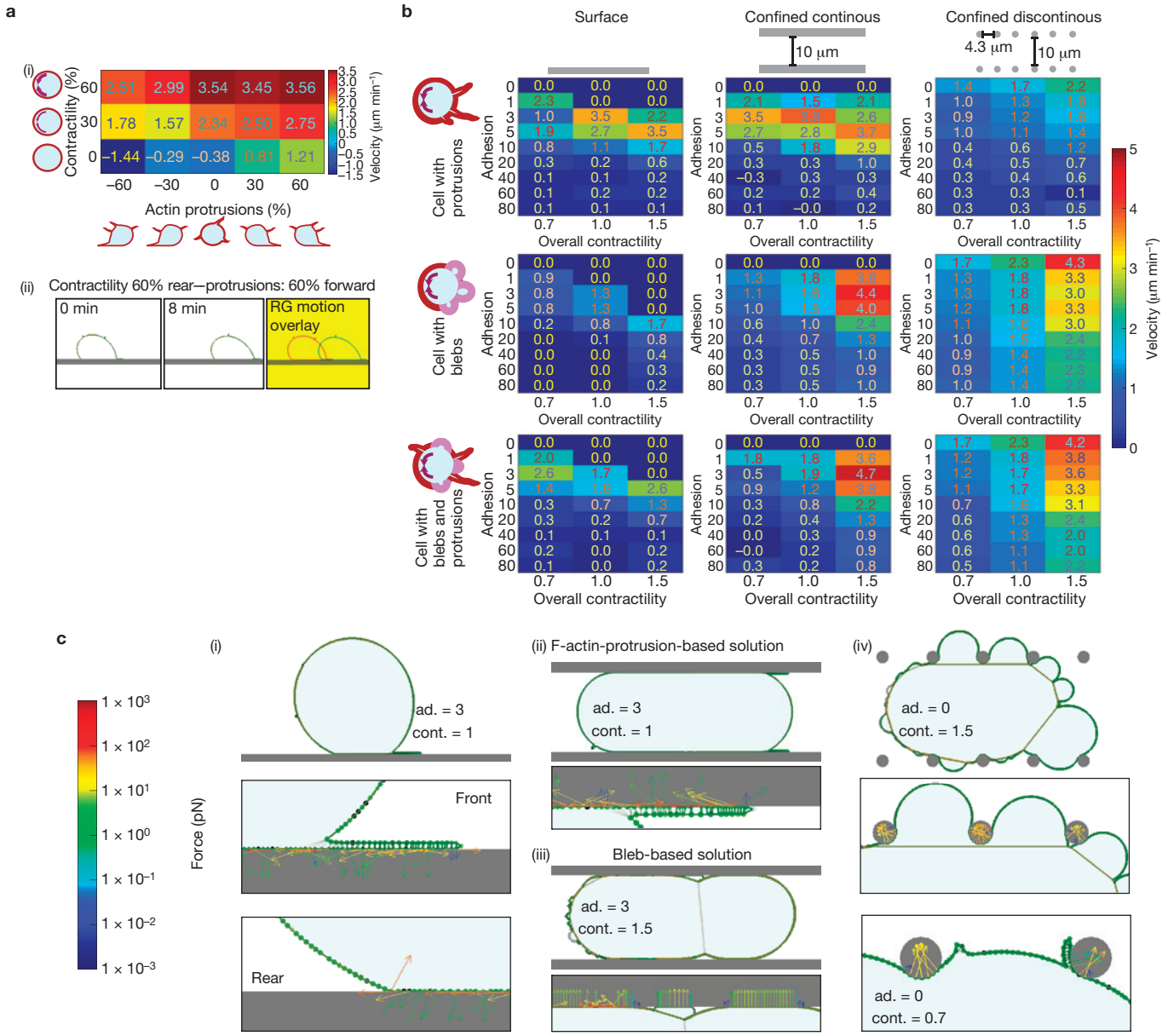

Figure 3 Different matrix geometries lead to different optimal migration strategies. (**a**) Velocity ($\mu m\,min^{-1}$) heat map for cell with variations in contractile and protrusion polarities. The *y* axis shows the level of contractility increase at the rear of the cell. The *x* axis shows the polarity in protrusion formation rate, as equivalent to corresponding myosin increase (Supplementary Fig. S2D). Negative values indicate that the protrusion rate is suppressed at the front of the cell, whereas positive values are suppression at the cell rear. Snapshot from the model of a cell crawling on a non-confined continuous surface, Supplementary Videos S3–S6. (**b**) Velocity heat maps of different cell mechanisms under changing adhesion and overall contractility levels. Columns, environments; rows, motility mechanisms. Within each plot: rows, adhesion to ECM (arbitrary units, see Supplementary Note—Adhesion mapping and atomic force microscopy simulations); columns, overall contractility. Where applicable, a polarity of 20% reduction in cortex–membrane linkers at the cell front, and a 30% increased polar contractility at the back, is imposed. Velocity ($\mu m\,min^{-1}$) colour bar is applicable to all plots. (**c**) Snapshots from motile cells in each environment; Supplementary Video S3. The colour coding is the same as in **a**. Insets demonstrate the forces applied by the cells to the environments; the colour bar at the left is valid for all insets. The adhesion (ad.) and overall contractility (cont.) of each snapshot are indicated. (i) Cell crawling on a surface; shown are the forces parallel to the direction of movement at the protruding front, and the pulling forces at the cell rear can be seen. (ii) The actin-protrusion-based solution within confined continuous environments, cell with overall contractility of 1.0, and forces acting on the surface in the protrusion region are demonstrated. (iii) Blebbing-driven solution for the same environment; overall contractility of the cell is 1.5. Forces applied on the surface are shown in the inset. (iv) Cell moving in a confined discontinuous environment, with zero cell–ECM adhesion. The cells can intercalate with the gaps of the ECM and have sufficient traction to move, using actin protrusions or blebs. The insets show the forces applied to the filaments by different types of protrusion.

to cause detachment of the cell from the matrix. This contrasts with the situation on unconfined surfaces where high levels of contractility lead to detachment, and not cell migration (Fig. 3b, Surface).

The level of confinement affects the balance between the beneficial effect of contractility, driving bleb formation, and the detrimental effect of high contractility on protrusion initiation.

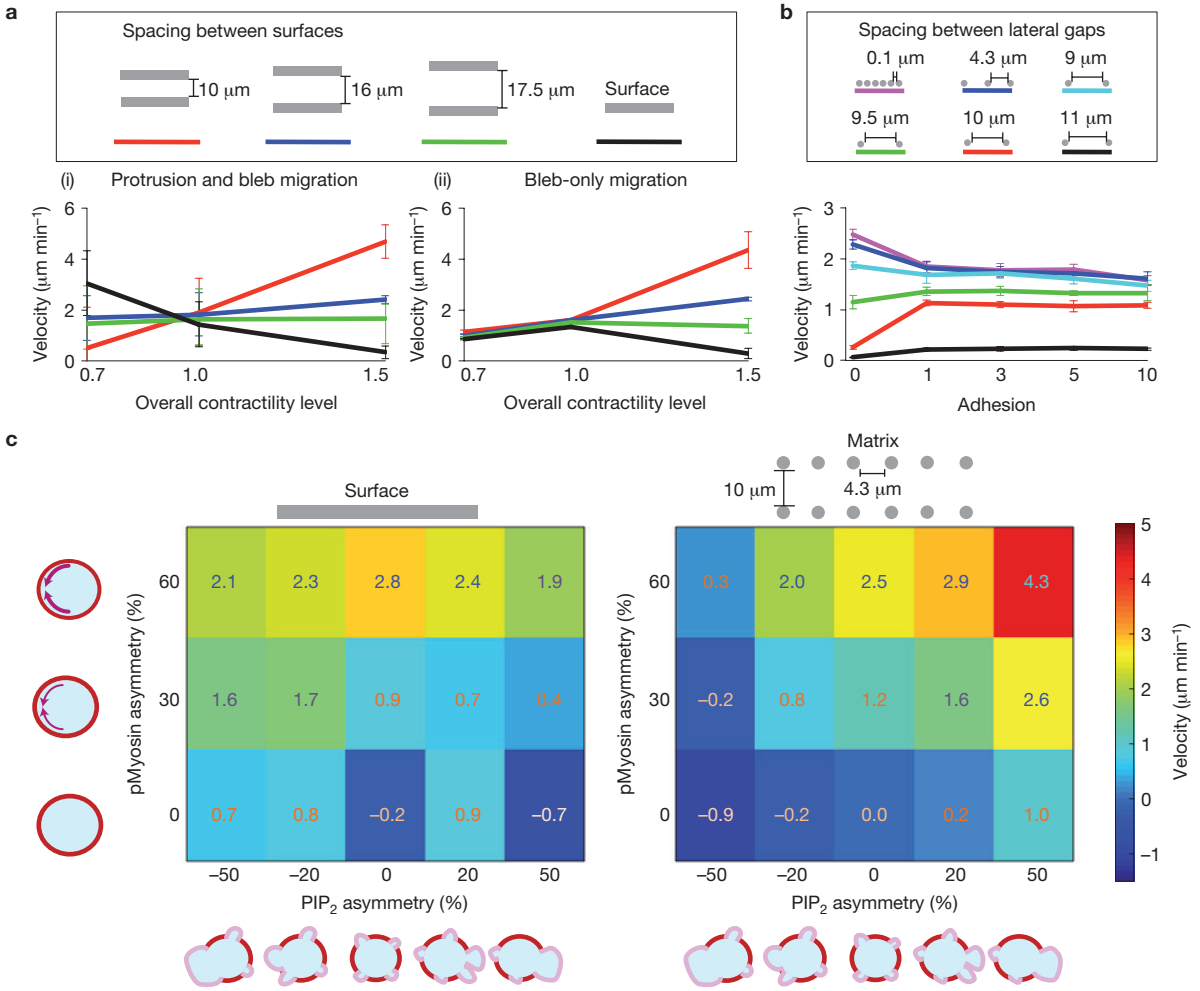

Figure 4 Effects of confinement and polarity on cell migration. (**a**) Velocity profiles at increasing overall contractility, for increasing confinement levels. (i) The cell is able to form protrusions and blebs. (ii) The cell can solely form blebs. (**b**) Velocity profile at increasing adhesion, and decreasing gap size on the sides of the cell's track. (**c**) Velocity heat maps for polarity alterations, rows: polarity in cortex–membrane linkers, the value is the percentage of reduction from the base level, negative sign indicates the cell rear, columns: polarity in contractility, the value indicates the percentage of increase over the base level, myosin increase is at the cell rear. The simulations are carried out at adhesion level 10 (for adhesion levels, see Supplementary Note—Adhesion mapping and atomic force microscopy simulations).

With increasing confinement, benefits of increased contractility dominate the profile (Fig. 4a, compare 17.5 μm and 16 μm with 10 μm). Investigating velocity profiles of solely bleb forming cells clearly demonstrates the altered contractility–velocity relationship with increasing confinement (Fig. 4a).

A discontinuous environment fundamentally alters the adhesion–velocity relationship

Changing the simulation environment to confined discontinuous matrix geometries results in total dominance of blebbing-based strategies. The critical importance of blebbing, as opposed to just high levels of actomyosin contractility, is demonstrated by higher velocities observed when blebbing is permitted compared with when it is prevented, even when contractility levels are equivalent (compare bottom right and top right matrices in Fig. 3b). Moreover, the adhesion dependence of the cell velocity profile is completely changed. Instead of an intermediate level of adhesion yielding the greatest cell velocity (Fig. 3b—left and middle matrices), the lower the cell–matrix adhesion values the higher the predicted velocity (Fig. 3b-right-hand matrices). Strikingly, this was maintained even when cell–matrix adhesion values of zero were used (Supplementary Video S6). The highly unusual nature of this result led us to investigate how the model could generate traction in the absence of cell–matrix adhesion. Observation of the model behaviour revealed that migration with cell matrix adhesion values set to zero was always associated with lateral expansions of the cell inter-digitating with the discontinuous matrix (Fig. 3c(iv) and Supplementary Video S6). Cell deformation around matrix structures generated a complex arrangement of forces. The magnitude of these forces was not greatly dependent on cell–matrix adhesions, indicating that the forces are generated by the moulding of the cell around the matrix and the resistance of the cell membrane, actin and cytoplasm to deformation (Fig. 3c(iv)). These lateral protrusions provide traction in the absence of adhesion, regardless of whether they were bleb-like or filopodial. Increasing the ECM gap size on the sides of the cell in the model leads to less effective inter-digitations and traction generation (Fig. 4b).

Thus, adhesion ceases to be a limiting factor within discontinuous confined environments.

Different asymmetries in contractility and cortex–membrane attachment are optimal depending on the matrix geometry

So far, we have linked asymmetry in contractility positively with asymmetry in cortex–membrane linkage. This was based on the following evidence: the rear of A375 cells is enriched for actomyosin and the actin–membrane linker proteins, Ezrin, Radixin and Moesin[9]. Also, higher levels of myosin function and PIP_2 are found at the rear of migrating cells[21]. However, there is no absolute reason why these parameters should be positively linked. Different studies have reported membrane blebs at the front, sides or rear of invading cells[9,10,12]. We investigated the consequences of locally varying the membrane–cortex linkage, and thereby biasing the likely location of blebs in the model (Fig. 4c). On non-confined surfaces, reduced cortex–membrane linkage at the rear increased cell speed, especially at lower levels of asymmetry in contractility (Fig. 4c left-hand matrix). In this situation, blebbing at the back of the cell facilitated its detachment and reduced the probability of protrusions at the cell rear. However, in discontinuous confined matrices, localized blebbing at the front is an effective way of pushing membrane and cytoplasm forward and lateral blebs can aid traction. Thus, higher cortex–membrane linkage at the rear of the cell is favourable in confined environments[9].

Model predicts *in vivo* behaviour of invasive melanoma cells

We next tested our model by trying to predict migratory behaviour in the discontinuous collagen-rich matrix that surrounds tumours. We therefore generated matrix geometries in the model that closely resembled the collagen-rich environment that surrounds melanoma. Second harmonic imaging of collagen fibres surrounding melanoma was used to determine the matrix structure that confronts melanoma cells[22]. The distribution of gaps between the fibres was then determined and a model matrix with a similar range of gap sizes was randomly generated (Supplementary Fig. S3A). These randomly generated matrices were termed *in vivo* mimetic matrices. The cell nucleus can hinder cell movement in 3D situations, and many of the gap sizes in the *in vivo* mimetic matrices are smaller than a cell nucleus[23–29]. To account for this, we added a nucleus to our model (Supplementary Fig. S3B, see Supplementary Note—Nucleus). The model nucleus is more rigid than the cytoplasm and the nuclear lamina is stiffer than the cell cortex[30,31]. Further, the nucleus can experience forces from the cortex (Supplementary Note—Nucleus). The behaviour of cells within the *in vivo* mimetic environment was then examined. First, we modelled the behaviour of A375P and A375M2 melanoma cells. A375M2 are a metastatic and invasive sub-line of A375P that have moderately increased myosin activity, elevated β_1 integrin expression and increased adhesion to collagen I (ref. 32; Table 1 and Supplementary Fig. S4A–E). A375M2 cells are predicted to have higher speeds than A375P when modelled in *in vivo* mimetic matrices (Supplementary Fig. S4F,G). In the *in vivo* mimetic matrix, membrane blebs, and not actin-polymerization-driven protrusions, were used to extend the cell forward (Fig. 5a and Supplementary Video S7). The blebs initially lacked F-actin, but polymerization of new F-actin subsequently restored the actin cortex. The bleb neck was disassembled by depolymerization. In many cases, the forward movement of the nucleus was prevented by the continued presence of the bleb neck. To determine whether depolymerization of the bleb neck represented a rate-limiting step we computationally modified the rate of bleb neck polymerization. This confirmed that faster rates of bleb neck depolymerization led to fast migration speeds (Supplementary Fig. S5A). Thus, our model predicts that A375M2 should utilize blebs to move and the bleb neck will interfere with the forward motion of the nucleus *in vivo*. We tested these predictions by performing intravital imaging of A375M2 melanoma cells invading into interstitial collagen. Tumours were generated using A375M2 cells expressing a fluorescent F-actin probe and labelled nuclei (Fig. 5b). Tumours were then imaged using multiphoton confocal microscopy and the F-actin organization and cell speed were analysed. Figure 5b shows an example of intravital imaging; motion of cells is highlighted by the overlay of images taken at different times in red, green and blue. Static cells appear white; moving cells appear coloured (Fig. 5b(ii)). Cells moved with broad rounded protrusions that initially lacked prominent F-actin (yellow arrow) but had a prominent F-actin neck at their base (magenta arrow). Depolymerization of the bleb neck (cyan arrow) was associated with forward movement of the nucleus. The importance of bleb neck depolymerization is highlighted by the lack of nuclear motion in cells that bleb, but do not depolymerize the bleb neck (contrast upper and lower cell in Supplementary Fig. S5B and Videos S8,S9). In the model, cycles of bleb formation and bleb neck depolymerization led to a saltatory type of migration with bursts of high centroid velocity interspersed with periods of almost stasis (Fig. 5a or c(i) and Supplementary Video S7). Instantaneous migration velocities observed *in vivo* were similar to those predicted and varied in a saltatory manner (Fig. 5c).

Table 1 Differences between A375P and A375M2 melanoma cells.

	F-actin protrusions	Actomyosin activity	Adhesion to collagen	Cortex–membrane attachment
A375P	1	1	1	1
A375M2—control	0.57	1.4	1.3	1

F-actin protrusions measured by F-actin staining, actomyosin activity by pS19-MYL9, adhesion to collagen measured directly and cortex–membrane attachment is measured by pERM. All reported values normalized to A375P cells. A375P-ECM adhesion strength is 10 adhesion units, see Supplementary Note—Adhesion mapping and atomic force microscopy simulations.

Bleb-driven migration strategies were faster over a large area of parameter space (Fig. 3b). This suggests that other cell types would exhibit similar behaviours at tumour margins. We therefore examined the behaviour of MDA-MB-231 breast cancer cells. F-actin protrusions, actomyosin contractility, phosphorylated Ezrin/Radixin/Moesin (Thr 567 in Ezrin) (pERM) levels and adhesion to collagen I were measured in MDA-MB-231 cells (relative to A375M2). The input values in the model were then adjusted to reflect the higher probability of F-actin protrusions, lower contractility and reduced cortex–membrane linkage in MDA-MB-231 cells (Supplementary Fig. S4H–N). In the model, these parameters predict that MDA-MB-231 cells would exhibit both F-actin protrusions and blebs *in vivo*, but the movement would be associated with forward-directed blebs (Supplementary Fig. S4m and Supplementary Video S10). Intravital imaging of MDA-MB-231 cells containing a fluorescent F-actin probe revealed the presence of both blebs and F-actin protrusions (Fig. 5d and Supplementary Video S11). In agreement with the model's prediction, moving cells had forward-directed blebs. Finally, we observed bleb-driven migration in primary explants of human squamous cell

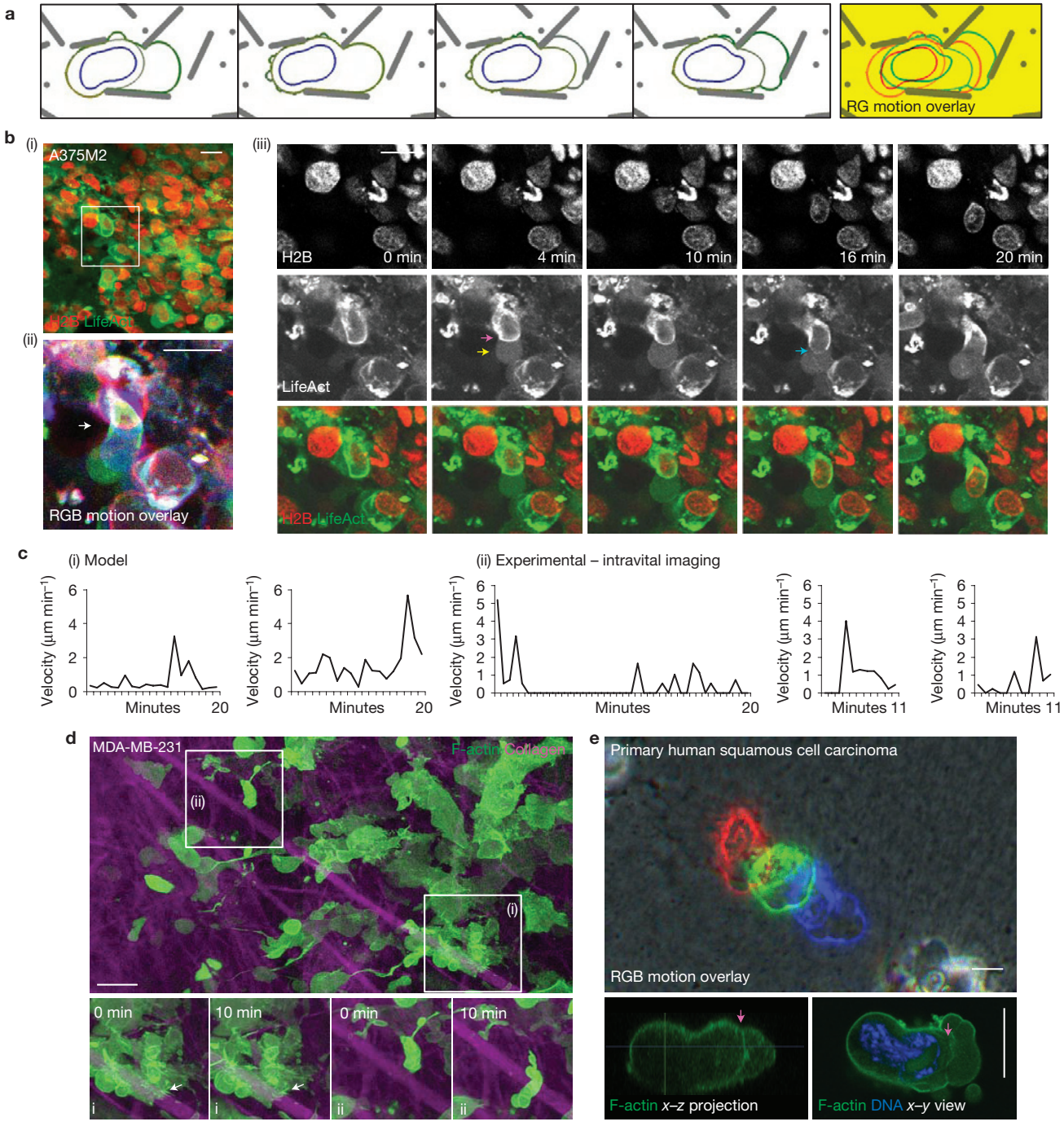

Figure 5 Blebbing migration dominates *in vivo*. (**a**) Representative still images from a simulation of an A375M2 cell moving through an *in vivo* mimetic matrix. Right panel: red–green (RG) motion overlay of the snapshots, demonstrating the pacing of the nucleus with the bleb neck, and consequent nucleus movement on disassembly of the neck. (**b**(i)) Representative 3D intravital image of LifeAct– (green) and H2B– (red) expressing A375M2 melanoma. (ii) Three single confocal LifeAct images of the area indicated in (i) are shown overlaid in red, blue and green. White indicates static cells whereas separate colours indicate motion. Each colour channel is separated by 6 min. (iii) LifeAct (green) and H2B (red) confocal sections of an A375M2 cell (highlighted with arrow in (ii)) moving *in vivo* at the indicated time points. Yellow arrow highlights bleb formation, magenta arrow shows bleb neck and cyan arrow indicates bleb neck depolymerization. Scale bars, 20 μm. (**c**(i)) Instantaneous velocities calculated at 60-second intervals of simulations for an A375M2 cell moving through a discontinuous 3D matrix—two representative simulations. (ii) Three examples of varying instantaneous velocity *in vivo*. (**d**) The large panel shows MDA-MB-231 cells expressing LifeAct (green) at the tumour margin (collagen SHG in magenta). Outlined areas are magnified to show (i) stationary behaviour of cells with F-actin protrusions (marked with arrow), and (ii) migration of MDA-MB-231 cell with blebs. Scale bar, 20 μm. (**e**) The large panel shows a red, green and blue overlay of a phase-contrast image of a migrating cell in a primary human tumour explant. Smaller panels show F-actin and nuclear staining in a fixed cell from the same explant. Scale bar, 10 μm. Bleb neck is highlighted with magenta arrow.

Table 2 The various experimental perturbations on A375M2 melanoma cells.

	F-actin protrusions	Actomyosin activity	Adhesion to collagen	Cortex–membrane attachment
A375M2 – control	0.57	1.4	1.3	1
A375M2 + Y3	0.87	0.85	1.3	0.93
A375M2 + Y10	2.8	0.78	1.3	0.85
A375M2 + dasatinib	0.14	1.8	1.3	1
A375M2 + ITGB1 dep	0.08	1.4	0.35	1
A375M2 + ITGB1 dep + Y3	1	1	0.35	0.93
A375M2 + ITGB1 dep + Y10	2.5	0.78	0.35	0.85
A375M2 + ITGB1 dep + dasatinib	0.13	1.8	0.35	1
A375M2 + ITGB1 and TLN dep	0.07	1.7	0.2	1
A375M2 + ITGB1 and TLN dep + Y3	0.62	1.4	0.2	0.93
A375M2 + ITGB1 and TLN dep + Y10	1.4	0.78	0.2	0.85
A375M2 + ITGB1 and TLN dep + dasatinib	0.1	1.8	0.2	1
A375M2 + dasatinib + Y3	1.8	1.1	1.3	0.93
A375M2 + dasatinib + Y10	3	0.78	1.3	0.85

F-actin protrusions measured by F-actin staining, actomyosin activity by pS19-MYL9, adhesion to collagen measured directly and cortex–membrane attachment is measured by pERM. All reported values normalized to A375P cells. A375P-ECM adhesion strength is 10 adhesion units, see also Supplementary Note—Adhesion mapping and atomic force microscopy simulations.

carcinoma in 3D cultures (Fig. 5e and Supplementary Video S12). These observations demonstrate the model's ability to predict the frequent use of bleb-driven migration by cancer cells.

Predicting the effect of experimental interventions in different matrix geometries

The data in Fig. 3b suggest that the same experimental perturbations might cause different effects on cell migration depending on the matrix geometry. Therefore, we sought to test our model by challenging it to predict the response of A375 cells to a divergent set of experimental perturbations in three different matrix geometries: on a planar substrate *in vitro*, confined between planar substrates *in vitro* and moving into interstitial collagen-rich matrices *in vivo*. We also picked three classes of manipulation: depletion of β_1 integrin or β_1 integrin and talin to reduce cell–matrix adhesion, inhibition of Rho-associated protein kinase (ROCK) using different doses of Y27632 to reduce contractility and inhibition of Src and other tyrosine kinases using dasatinib to disrupt signalling from cell–matrix adhesions to cell protrusion and contractility regulators. To rigorously explore the predictive power of the model, we tested multiple combinations of the manipulations in the different matrix geometries (36 combinations in total). The effect of these manipulations on F-actin protrusion, cortical contractility, β_1 integrin expression, adhesion to collagen I and cortex–membrane attachment was determined experimentally *in vitro* on 2D substrates (Supplementary Fig. S6A–G). Only these *in vitro* 2D measurements were used in the model to predict behaviour both in non-confined and confined *in vitro* environments and complex *in vivo* environments. Table 2 summarizes how the various manipulations affected cell protrusions, actomyosin contractility, β_1 integrin levels and membrane–cortex attachment (as measured by the surrogate pERM). Our model predicts different effects of these perturbations on cell migration depending on matrix geometry. Both Y27632 treatment (reduced contractility) and β_1 integrin depletion are predicted to reduce migration on a continuous planar surface (Fig. 6b(i) or Supplementary Fig. S7Ai). However, only Y27362 treatment is predicted to reduce migration in all the environments. β_1 Integrin depletion is predicted to increase cell speed in confined continuous environments. The effects of combinatorial manipulations are also predicted to be highly divergent dependent on the matrix geometry. Y27632 treatment is predicted to negate the effect of integrin depletion on 2D surfaces. This reflects the observation that adhesion and contractility scale together to yield optimal migration speeds on planar surfaces (Fig. 3b). However, in confined environments the effects of contractility dominate in the model, leading to the prediction that Y27632 treatment will reduce migration, even in β_1 integrin-depleted cells. Dasatinib, which increases contractility, was predicted to lead to variable cell behaviour. On 2D surfaces, cells with moderately elevated contractility at their rear would move with a rounded morphology, but cells with greater contractility at their rear would begin to detach and move very little (Supplementary Fig. S6Ai compare top and bottom panel). In contrast, dasatinib treatment was not predicted to have pronounced effects in confined continuous or *in vivo* environments.

We tested these predictions by measuring A375M2 cell migration following experimental perturbation in the differing matrix environments. For *in vitro* analysis, A375M2 cells were plated on collagen I, or between two collagen-coated surfaces separated by 10–11 μm beads (thereby generating a confined environment), and the migration efficiency was monitored by time-lapse microscopy (Fig. 6a). *In vivo* predictions were tested by the injection of control A375M2 or β_1 integrin short hairpin RNA (shRNA) A375M2 cells and treating mice with Y27632 or dasatinib. As predicted by our model, inhibition of ROCK kinases or depletion of β_1 integrin reduced cell migration on a planar surface. Several other predictions were also confirmed. First, β_1 integrin depletion increased cell speed in confined continuous environments but had little effect *in vivo*. Second, and most strikingly, the combination of β_1 integrin depletion and Y27632 treatment had very different consequences depending on the matrix geometry. On 2D surfaces, migration velocities were similar to controls (even though either treatment alone significantly reduced motility), whereas in confined environments the effect of ROCK inhibition dominated and Y27632 treatment reduced cell migration in β_1 integrin-depleted cells. Finally, dasatinib treatment led to more variable cell behaviour on 2D surfaces, with rounded cells either moving rapidly or being stationary, but had little effect in confined environments (Fig. 6b).

The model performed well across the range of conditions that we investigated. The overall correlation between computationally predicted effects and experimentally observed effects was $r = 0.63$, $P < 0.0001$ (Fig. 6c). The utility of the model is demonstrated by contrasting the simple extrapolation of the effects observed on a planar

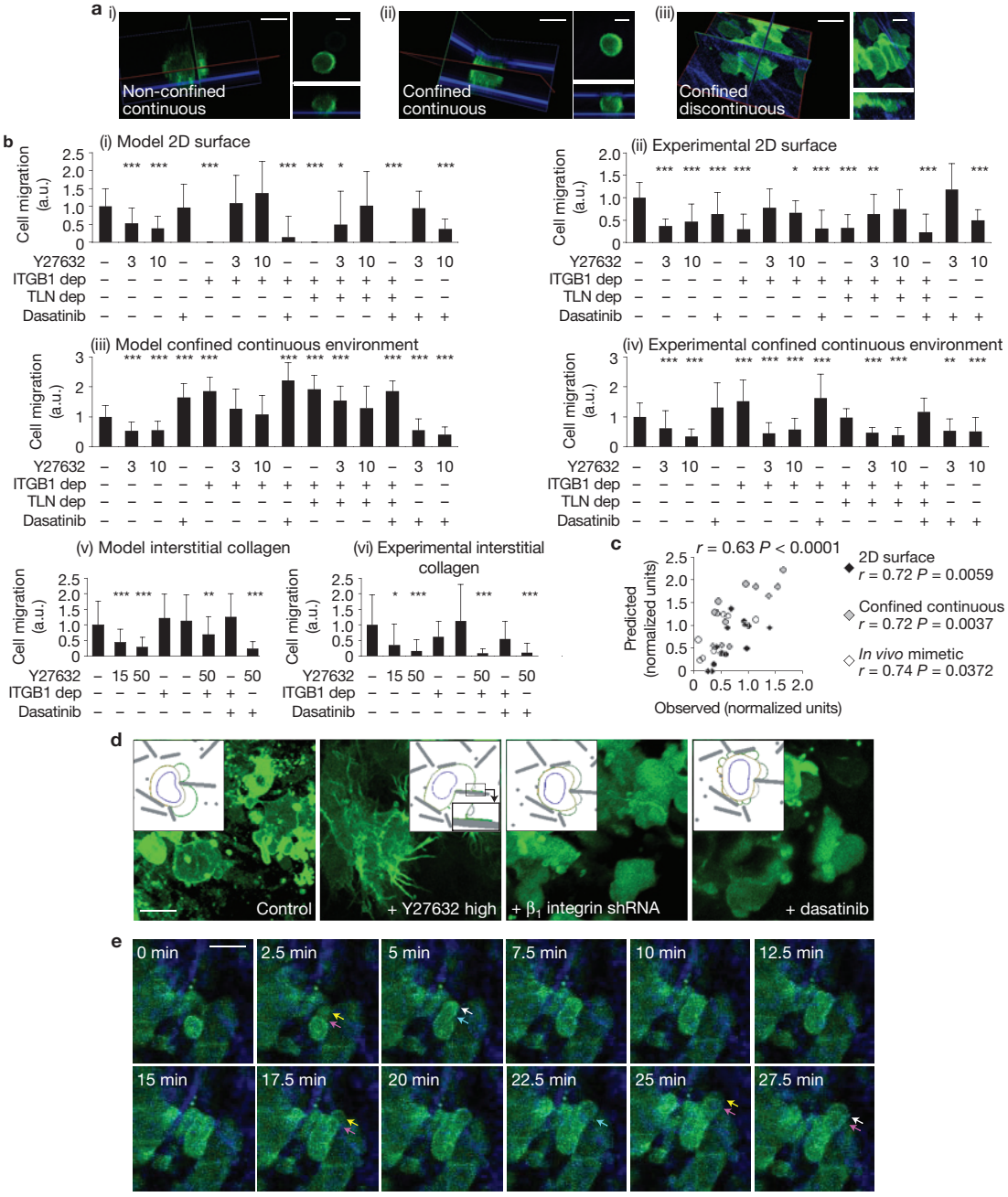

Figure 6 Model predicts effects on perturbations in different matrix environments. (**a**) Three experimental contexts used to test the model; matrix in blue and cells in green. Left panels show 3D reconstruction, middle panels show *y*–*z* projection (green plane in 3D reconstructions) and right panels show *x*–*y* projection (red plane in 3D reconstruction). Scale bars, 10 μm. (**b**(i) and (iii)) Model-predicted changes in cell migration caused by the experimental manipulations if a cell is moving on a 2D continuous surface or between two continuous surfaces with a 12.5 μm gap in between ($n = 30$ independent simulations for each point, error bars: one standard deviation). (ii) and (iv) Experimental measurements of A375M2 cells moving on a collagen surface, or sandwiched in between collagen surfaces ($n \geq 23$ cells, *n* values for each data point are given in Supplementary Table S4—Statistics Source Data). (v) and (vi) Model predictions on changes in cell migration caused by experimental manipulations within a discontinuous 3D matrix, and the corresponding experimental measurements of A375M2 cells moving into interstitial collagen *in vivo*. Computational analysis, $n = 90$ for each data point, error bars: standard deviation. *In vivo* analysis is from intravital imaging of $n = 55$, 15, 31, 18, 14, 15, 10 and 20 tumour volumes for control, Y27632 low, Y27632 high, β_1 integrin-shRNA-treated, dasatinib-treated, β_1 integrin + Y27632 high, β_1 integrin + dasatinib, and Y27632 high + dasatinib tumours, respectively. Values are normalized to aid comparison. See also Supplementary Fig. S5. Significant differences from the control under the same conditions are marked (two-tailed *t*-test, * indicates *P* value < 0.05, ** *P* value < 0.01, *** *P* value < 0.001). (**c**) The scatter plot of experimentally observed and computationally predicted changes in cell migration. Pearson correlation coefficients and significance values are shown. (**d**) Representative images show F-actin organization (in green) *in vivo* following experimental perturbation. Inset panels show representative snapshots from the computational model. Scale bar, 20 μm. (**e**) LifeAct–GFP (green) expressed in A375M2 β_1 integrin shRNA cells and collagen second harmonic generation (blue). Yellow arrow shows F-actin poor bleb initiation, white arrow indicates new F-actin polymerization in the bleb, magenta arrow shows bleb neck and cyan arrow indicates bleb neck disappearance. Scale bar, 20 μm.

surface to confined continuous or *in vivo* situations. Extrapolation of the 2D experiments to a confined continuous environment or the *in vivo* situation yields no significant relationship ($r = -0.43$, $P = 0.12$ and $r = 0.07, P = 0.86$, respectively (Supplementary Fig. S7Ci and Cii)). In contrast, the predictions of the model yield a significantly positive relationship with experimentation both in *in vitro* confined continuous environments ($r = 0.72$, $P = 0.004$) and *in vivo* ($r = 0.74$, $P = 0.04$; Fig. 6c).

Finally, we examined morphological features predicted by our model *in vivo*. ROCK inhibition was predicted to increase protrusions and reduce blebbing, whereas dasatinib would be associated with chaotic blebbing behaviour (Fig. 6d, inset). Imaging confirmed the accuracy of these predictions (Fig. 6d). β_1 Integrin-depleted cells were predicted to migrate by the same bleb-driven mechanism as control cells. Figure 6e shows *in vivo* imaging of the actin organization in a migrating β_1 integrin-depleted cell. Repeated cycles of bleb initiation, new polymerization of the cortex, and bleb neck dissolution are clearly observed (Fig. 6e, Supplementary Video S13): thus, the model accurately predicts both quantitative changes in cell migration and the qualitative mechanism of cell migration.

DISCUSSION

The multi-scale model of cancer cell motility presented here incorporates actin-polymerization-based protrusions, contractility, blebbing, the cell nucleus, variable ECM attachment and variable ECM topology in a cell motility context. Although models for actin-polymerization-driven protrusions or single bleb initiation have been described previously[14,15,17,18], our model relates both phenomena to cell motility. The model is constructed using experimental data solely obtained *in vitro*, and the emergent behaviour of the simulations strongly mimics and predicts cell behaviour *in vitro* and *in vivo*.

Confinement alters the relationship between contractility and velocity. Confined environments favour higher levels of contractility. This is caused by two factors: confinement reduces the ability of high contractility to reduce cell velocity owing to the cells detaching from the ECM, and it enables hydrostatic pressure to drive bleb formation more effectively when contractility is increased. We use a confined continuous environment to demonstrate the dominant effects of manipulating contractility over changes in adhesion. Further, increased matrix density leads to increasing reliance on contractile myosin function in dendritic cells[13]. In confined continuous environments, two effective solutions are observed: an F-actin protrusion-driven, moderate contractility mechanism; and a high contractility, blebbing mechanism. Our model predicts that protrusions can reduce hydrostatic pressure and thereby reduce blebbing. This provides a physical mechanism of bistability and reduces interconversion between migration strategy. This is likely to function in parallel with Rho–Rac inhibitory crosstalk.

In confined but discontinuous environments the relationship between adhesion and velocity is changed. Instead of a bell-shaped relationship, reducing adhesion simply increases velocity. At low or zero cell–matrix adhesion the source of traction becomes the inter-digitation of actin protrusions or blebs into gaps in the matrix. The forces experienced by these structures result from the resistance of the cell cortex and cytoplasm to deformation. A wide range of gap sizes smaller than the approximate radius of the cell can be used (Fig. 4c). Much evidence supports this analysis: β_1 integrin depletion has no effect on A375M2 migration into interstitial collagen. Further, depletion of all integrins does not perturb dendritic cell migration *in vivo*[13]. These experimental analyses cannot exclude a role for other matrix-binding molecules[33], but our model enables us to conclude that cell migration can be entirely adhesion independent in certain matrices. Although, we did not observe matrix fibre deformation in our intravital analysis, it is possible that small ($>1\,\mu m$) deformations in collagen fibres might affect the performance of our model. However, when we additionally considered the flexibility of the matrix, key predictions of our model regarding *in vivo* cell migration were unaltered (Supplementary Fig. S7).

Blebbing-driven migration is predicted to be the most rapid form of migration in discontinuous environments. Although many studies have observed blebbing during cell migration, its role has remained contentious[1,8,11]. Depending on the system, blebbing has been observed at the front, side and rear of migrating cells, leading to the proposition that it is merely a consequence of cortical contractility with no actual utility[9,10,12]. Our computational model allows us to explore suppression of blebbing without altering contractility or the spatial relationship of blebbing to the direction of migration. Forward blebbing is an effective method for cell protrusion in confined spaces, but on planar surfaces small blebs at the rear can favour detachment.

By exploring parameter space we can determine which parameters have the largest effects on cell migration depending on the matrix geometry. This will enable more efficient targeting to identify anti-invasive chemotherapeutic agents. By measuring simple variables *in vitro*, we have been able to predict the *in vivo* efficacy of three very different putative anti-invasive interventions. We believe that our model can be a useful tool to aid more rational drug screening approaches and to determine the likely context in which anti-migration agents might act. □

METHODS

Methods and any associated references are available in the online version of the paper.

Note: Supplementary Information is available in the online version of the paper

ACKNOWLEDGEMENTS

We would like to thank R. Chaleil for his support and maintenance of the high-performance computing system, A. Weston for electron microscopy, and numerous colleagues for advice and constructive critiques.

AUTHOR CONTRIBUTIONS

M.T., P.A.B. and E.S. designed the study; M.T. and A.L.T. implemented the computer algorithms; E.S. and S.H. designed and constructed the cell-based assays and *in vivo* experiments; R.P.J. carried out image analysis and quantification; M.T., A.L.T., P.A.B. and E.S. analysed and discussed the results; all authors contributed to the writing of the manuscript.

COMPETING FINANCIAL INTERESTS

The authors declare no competing financial interests.

Published online at www.nature.com/doifinder/10.1038/ncb2775
Reprints and permissions information is available online at www.nature.com/reprints

1. Sahai, E. & Marshall, C. J. Differing modes of tumour cell invasion have distinct requirements for Rho/ROCK signalling and extracellular proteolysis. *Nat. Cell Biol.* **5,** 711–719 (2003).
2. Wolf, K. *et al.* Compensation mechanism in tumor cell migration: mesenchymal-amoeboid transition after blocking of pericellular proteolysis. *J. Cell Biol.* **160,** 267–277 (2003).

3. Sanz-Moreno, V. *et al*. Rac activation and inactivation control plasticity of tumor cell movement. *Cell* **135,** 510–523 (2008).
4. Carragher, N. O. *et al*. Calpain 2 and Src dependence distinguishes mesenchymal and amoeboid modes of tumour cell invasion: a link to integrin function. *Oncogene* **25,** 5726–5740 (2006).
5. Charras, G., Yarrow, J., Horton, M., Mahadevan, L. & Mitchison, T. J. Non-equilibration of hydrostatic pressure in blebbing cells. *Nature* **435,** 365–369 (2005).
6. Otto, A., Collins-Hooper, H., Patel, A., Dash, P. R. & Patel, K. Adult skeletal muscle stem cell migration is mediated by a blebbing/amoeboid mechanism. *Rejuvenation Res.* **14,** 249–260 (2011).
7. Kardash, E. *et al*. A role for Rho GTPases and cell–cell adhesion in single-cell motility *in vivo*. *Nat. Cell Biol.* **12,** 47–53 (2009).
8. Blaser, H. *et al*. Migration of zebrafish primordial germ cells: a role for myosin contraction and cytoplasmic flow. *Dev. Cell* **11,** 613–627 (2006).
9. Lorentzen, A., Bamber, J., Sadok, A., Elson-Schwab, I. & Marshall, C. An ezrin-rich, rigid uropod-like structure directs movement of amoeboid blebbing cells. *J. Cell Sci.* **124,** 1256–1267 (2011).
10. Poincloux, R. *et al*. Contractility of the cell rear drives invasion of breast tumor cells in 3D Matrigel. *Proc. Natl Acad. Sci. USA* **108,** 1943–1948 (2011).
11. Trinkaus, J. P. Formation of protrusions of the cell surface during tissue cell movement. *Prog. Clin. Biol. Res.* **41,** 887–906 (1980).
12. Estecha, A. *et al*. Moesin orchestrates cortical polarity of melanoma tumour cells to initiate 3D invasion. *J. Cell Sci.* **122,** 3492–3501 (2009).
13. Lammermann, T. *et al*. Rapid leukocyte migration by integrin-independent flowing and squeezing. *Nature* **453,** 51–55 (2008).
14. Ly, D. & Lumsden, C. 3D amoeboid migration of a eukaryotic cell in a fiber matrix. *Artif. Life Robot.* **14,** 1–6 (2009).
15. Neilson, M. *et al*. Chemotaxis: a feedback-based computational model robustly predicts multiple aspects of real cell behaviour. *PLoS Biol.* **9,** e1000618 (2011).
16. Hawkins, R. J. *et al*. Pushing off the walls: a mechanism of cell motility in confinement. *Phys. Rev. Lett.* **102,** 058103 (2009).
17. Young, J. & Mitran, S. A numerical model of cellular blebbing: a volume-conserving, fluid-structure interaction model of the entire cell. *J. Biomech.* **43,** 210–220 (2010).
18. Tinevez, J-Y. *et al*. Role of cortical tension in bleb growth. *Proc. Natl Acad. Sci. USA* **106,** 18581–18586 (2009).
19. Bagorda, A. & Parent, C. A. Eukaryotic chemotaxis at a glance. *J. Cell Sci.* **121,** 2621–2624 (2008).
20. Rorth, P. Whence directionality: guidance mechanisms in solitary and collective cell migration. *Dev. Cell* **20,** 9–18 (2011).
21. Iijima, M., Huang, Y. E., Luo, H., Vazquez, F. & Devreotes, P. Novel mechanism of PTEN regulation by its phosphatidylinositol 4,5-bisphosphate binding motif is critical for chemotaxis. *J. Biol. Chem.* **279,** 16606–16613 (2004).
22. Wolf, K. *et al*. Collagen-based cell migration models *in vitro* and *in vivo*. *Semin. Cell Dev. Biol.* **20,** 931–941 (2009).
23. Wolf, K. & Friedl, P. Mapping proteolytic cancer cell-extracellular matrix interfaces. *Clin. Exp. Metastasis* **26,** 289–298 (2009).
24. Sims, J. R., Karp, S. & Ingber, D. E. Altering the cellular mechanical force balance results in integrated changes in cell, cytoskeletal and nuclear shape. *J. Cell Sci.* **103,** 1215–1222 (1992).
25. Yamauchi, K. *et al*. Real-time *in vivo* dual-color imaging of intracapillary cancer cell and nucleus deformation and migration. *Cancer Res.* **65,** 4246–4252 (2005).
26. Nakayama, M. *et al*. Rho-kinase and myosin II activities are required for cell type and environment specific migration. *Genes Cell.* **10,** 107–117 (2005).
27. Bellion, A., Baudoin, J-P., Alvarez, C., Bornens, M. & Métin, C. Nucleokinesis in tangentially migrating neurons comprises two alternating phases: Forward migration of the Golgi/centrosome associated with centrosome splitting and myosin contraction at the rear. *J. Neurosci.* **25,** 5691–5699 (2005).
28. Tsai, J-W., Bremner, H. & Vallee, R. Dual subcellular roles for LIS1 and dynein in radial neuronal migration in live brain tissue. *Nature Neurosci.* **10,** 970–979 (2007).
29. Beadle, C. *et al*. The role of myosin II in glioma invasion of the brain. *Mol. Biol. Cell* **19,** 3357–3368 (2008).
30. Guilak, F., Tedrow, J. & Burgkart, R. Viscoelastic properties of the cell nucleus. *Biochem. Biophys. Res. Commun.* **269,** 781–786 (2000).
31. Caille, N., Thoumine, O., Tardy, Y. & Meister, J-J. Contribution of the nucleus to the mechanical properties of endothelial cells. *J. Biomech.* **35,** 177–187 (2002).
32. Clark, E. A., Golub, T. R., Lander, E. S. & Hynes, R. O. Genomic analysis of metastasis reveals an essential role for RhoC. *Nature* **406,** 532–535 (2000).
33. Hegerfeldt, Y., Tusch, M., Brocker, E. B. & Friedl, P. Collective cell movement in primary melanoma explants: plasticity of cell–cell interaction, beta1-integrin function, and migration strategies. *Cancer Res.* **62,** 2125–2130 (2002).

METHODS

The model. Representation of a cell body *in silico* has taken many forms: point representation of cells[34], definition of cell morphology with predefined shape or tessellation[35–37], definition of flexible morphology using grid-based models[38,39] or continuous 3D representation of cell shape and volume[40]. In addition, simple finite-element representations have been used alone or in conjunction with other modelling techniques[41–43]. In a recent work, we used an agent-based model for definition of cell morphologies in a simulation study of early-stage vascularization[44]. Modelling the amoeboid cell requires a method that can take account of both global and local cellular properties in a continuous space. Moreover, as we aim to investigate a complex system of biophysical interactions within the cell and between the cell and the extracellular matrix, we need a computationally efficient method. Hence, we developed a 2D hybrid agent-based/finite-element model of amoeboid cancer cell motility within a set of variable ECM topologies. Details of the modelling methodology are thoroughly explained in Supplementary Note. The parameters used in the model are listed in Supplementary Table S1, and the definition of all the modelling nomenclature is given in Supplementary Table S3.

Experimental methods—intravital imaging. Female 6–10-week-old nude mice were either injected subcutaneously with 10^6 A375M2 melanoma cells or injected under the fourth nipple with 10^6 MDA-MB-231 breast cancer cells. When tumours were 5–11 mm, mice were anaesthetized using 3–5% isofluorane in oxygen and the skin over-lying the tumour was surgically displaced. The mice were placed on a Zeiss LSM780 confocal microscope with a pulsed Ti:sapphire laser and imaged using either a ×20 0.8 NA objective or a ×63 1.2 NA objective. Either 15 mg kg^{-1} or 50 mg kg^{-1} (low and high dose, respectively) Y27362 in saline was administered 90 min before imaging by intraperitoneal injection. Dasatinib (10 mg kg^{-1}) freshly prepared in 10% DMSO and 90% saline was administered 90 min before imaging by oral gavage. Anaesthesia was maintained using 1.5–2.5% isofluorane in oxygen throughout imaging. A heated stage and blanket were used to counteract the possible hypothermic effects of the anaesthetic. Work performed under licence PPL80/2368.

Typically, several tumour areas were imaged per mouse. Quantification was performed by scoring the number of moving melanoma cells per tumour area. Details are provided in the Statistics Source Data file. All cells were scored, regardless of blebbing behaviour. In fact, almost all of the movies used for quantification were of a resolution too low to permit clear determination of cell blebbing.

Experimental method—cell culture A375P and A375M2 cells were routinely maintained in DMEM + 10% fetal calf serum[32]. Transfection of MARS–LifeAct, GFP–LifeAct, EGFP–N1 Ezrin, EGFP–N3 MYL9, EGFP–PLCδPH domain and pNeo β_1 integrin shRNA plasmids was carried out using a plasmid DNA concentration of 2 μg ml^{-1} and Fugene6 diluted 6:1,000 in Optimem. In the case of LifeAct plasmids and pNeo β_1 integrinshRNA, stable transfectants were selected using 500 μg ml^{-1} geneticin and purified by FACS. The siRNA and shRNA sequences for β_1 integrin are described in ref. 45.

Experimental method—immunofluorescence. Cells were plated on collagen I (∼4.5 mg ml^{-1}; BD Bioscience, #354249) and were cultured in serum-free media for 4–6 h before measurement of their cytoskeletal properties. Cells were fixed with 4% paraformaldehyde, permeabilized with 0.2% Triton X-100 and blocked with 5% BSA. Primary antibodies (phospho-Ezrin (Thr 567)/Radixin (Thr 564)/Moesin (Thr 558) antibody—Cell Signaling #3141, phospho-Src family (Tyr 416)—Cell Signaling #2101, phospho-Myosin Light Chain 2 (Ser 19)—Cell Signaling #3671, and P5D2 β_1 integrin Santa Cruz sc-13590) were diluted 1:100 and incubated overnight at 4 °C and secondary antibodies (Cy5 anti-rabbit, Jackson Stratech, and Alexa 488 anti-mouse) and TRITC–phalloidin were incubated for 1 h at room temperature. Images were acquired using Zeiss LSM confocal systems. To quantify pS19-MYL9 and β_1 integrin staining images were opened in Volocity. Cells were identified by thresholding based on F-actin staining intensity and selected on the basis of area >200 μm. Mean fluorescent intensities were determined for each cell.

Experimental method—adhesion assays. Cells removed were non-ezymatically detached (using Gibco-BRL #13150-016) before re-plating on dishes coated with 0.1 mg ml^{-1} collagen. Thirty minutes later, non-adherent cells were removed by tipping the media out and washing three times with PBS. Adherent cells were then fixed using 4% PFA and the number of cells in three ×20 fields was counted. In addition, one dish was allowed to adhere for 12 h before fixation. This was used to determine the total number of viable cells originally added to the dishes. The number of adherent cells after 30 min was then divided by the number of viable cells. In Supplementary Fig. S4c the values were normalized to A375P cells, in other figures the values were normalized to A375M2.

Experimental method—time-lapse imaging. To investigate cytoskeletal dynamics, A375 cells were plated on collagen I (∼4.5 mg ml^{-1}; BD Bioscience, #354249) and then transferred to serum-free media. In some cases, cell behaviour was modulated by the addition of 1% serum (1/100 volume of pure serum), 3 μM Y27632, 10 μM Y27632 (Tocris #1254), 300 nM dasatinib, 1 μM dasatinib (LCLlabs #3307) or combinations thereof. *In vitro* time-lapse imaging was performed at 37 °C using a range of platforms: Nikon TE2000 microscopes equipped with environmental chambers and a CCD (charge-coupled device) controlled by MetaMorph software or Zeiss LSM confocal microscopes (either LSM510, 710 or 780). Frame acquisition rates ranged from 1 to 0.25 Hz.

To study cell migration we used collagen-coated coverslips. For 2D continuous non-confined environments we used 12-well MatTek dishes coated with a 0.1 mg ml^{-1} solution of collagen I (Advanced BioMatrix #5005-B). A375M2 cells were imaged plated in Liebowitz media (Invitrogen #21083-027) containing 0.1% FCS and 5 ng ml^{-1} HGF (Sigma H9661) (100 μl bead suspension + 400 μl cell suspension). Imaging was performed using Nikon TE2000 microscopes equipped with environmental chambers and a CCD controlled by MetaMorph software. To generate a confined continuous environment with defined spacing we used 12-well MatTek dishes and 12 mm round glass coverslips coated with a 0.1 mg ml^{-1} solution of collagen I. A suspension of 10–11 μm polystyrene beads (Invitrogen #F13838) in PBS was then prepared and mixed with a suspension of A375M2 cells in Liebowitz media (Invitrogen #21083-027) containing 0.1% FCS and 5 ng ml^{-1} HGF (Sigma H9661) (100 μl bead suspension + 400 μl cell suspension). This was then placed in the 12-well MatTek dish and the beads and cells were allowed to settle for 10 min. A collagen-coated glass coverslip was then lowered on the MatTek dish and gently pushed down. A large number of beads and cells then become confined between the bottom of the MatTek dish and the coverslip. Additional 4 mm glass beads (ThermoFisher #10735331) were added on top to weight the coverslip down. The efficacy of the procedure was then confirmed by confocal reflectance microscopy before time-lapse imaging.

Experimental method—western blotting. Lysates were prepared in Laemlli buffer (without β-mercaptoethanol for β_1 integrin analysis). Following standard SDS–PAGE, proteins were transferred to nitrocellulose/PVDF membranes and incubated with the following primary antibodies (all diluted 1:1,000, except tubulin 1:20,000): phospho-Ezrin (Thr 567)/Radixin (Thr 564)/Moesin (Thr 558) antibody—Cell Signaling #3141, phospho-Src family (Tyr 416)—Cell Signaling #2101, phospho-Myosin Light Chain 2 (Ser 19)—Cell Signaling #3671, Talin antibody (clone 8D4)—Santa Cruz sc-5988, anti-β-Tubulin I—Sigma T7816, β_1 integrin—Santa Cruz sc-13590 (clone P5D2), and β_1 integrin—Millipore MAb1965 (clone JB1a).

Experimental method—acquiring the data for parameterisation. The quantification of pS19-MYL9 was performed using Volocity software. Briefly, images were thresholded using F-actin staining and individual cells automatically detected. The thresholded F-actin image was then used as a mask to quantify the average pS19-MYL9 fluorescent intensity in each cell. Cell-membrane attachment was quantified using fluorescent intensity measurements of pERM staining (in this case, the cell shapes were manually traced because the 10% TCA fix used is not compatible with F-actin staining and automated F-actin thresholding). We additionally used western blotting of whole-cell lysates to confirm that pERM levels did not vary greatly. The protrusion initiation probability was determined by sampling eight points around the cell border (an octagon was fitted to the cell and the corners were used as the eight points). Each point was then scored for the presence or absence of an F-actin protrusion, giving a score from 0 to 8. This was then divided by 4 to approximate the probability that a cross-section through the cell would have a protrusion on one side (value = 1), on both sides (value = 2) or not at all (value = 0).

The distributions of pS19-MYL9 and pERM approximate to normal distributions. The variation observed reflects the heterogeneity observed within the population of cells and is not the result of inaccurate measurements. The mean value was used for model parameterization. In addition, the model is always run with three slightly different levels of asymmetry, and because the asymmetry is calculated as an increase relative to the mean in one of the cells, this means that three slightly different levels of actomyosin activity and cell-membrane attachment are evaluated. The main figures show the model output for the average of the three slightly different runs. The supplementary figures show the model output for each of the individual sets of runs (Supplementary Figs S4F, S7A, S8K).

DOI: 10.1038/ncb2775

34. Zaman, M., Kamm, R., Matsudaira, P. & Lauffenburger, D. Computational model for cell migration in three-dimensional matrices. *Biophys. J.* **89,** 1389–1397 (2005).
35. Beyer, T. & Meyer-Hermann, M. Multiscale modeling of cell mechanics and tissue organization. *IEEE Eng. Med. Biol. Magaz.* **28,** 38–45 (2009).
36. Mao, Y. *et al.* Planar polarization of the atypical myosin Dachs orients cell divisions in *Drosophila*. *Genes Dev.* **25,** 131–136 (2011).
37. Eisenmann, K.M. *et al.* T cell responses in mammalian diaphanous-related formin mDia1 knock-out mice. *J. Biol. Chem.* **282,** 25152–25158 (2007).
38. Anderson, , Chaplain, & Rejniak, *Single-Cell-Based Models in Biology and Medicine (Mathematics and Biosciences in Interaction)* (Birkhäuser, 2007).
39. Maree, A., Jilkine, A., Dawes, A., Grieneisen, V.n. & Edelstein-Keshet, L. Polarization and movement of keratocytes: a multiscale modelling approach. *Bull. Math. Biol.* **68,** 1169–1211 (2006).
40. Herant, M. & Dembo, M. Cytopede: a three-dimensional tool for modeling cell motility on a flat surface. *J. Comput. Biol.* **17,** 1639–1677 (2010).
41. Bottino, D., Mogilner, A., Roberts, T., Stewart, M. & Oster, G. How nematode sperm crawl. *J. Cell Sci.* **115,** 367–384 (2002).
42. Pappu, V., Doddi, S. & Bagchi, P. A computational study of leukocyte adhesion and its effect on flow pattern in microvessels. *J. Theoret. Biol.* **254,** 483–498 (2008).
43. Rejniak, K. An immersed boundary framework for modelling the growth of individual cells: an application to the early tumour development. *J. Theoret. Biol.* **247,** 186–204 (2007).
44. Bentley, K., Mariggi, G., Gerhardt, H. & Bates, P. A. Tipping the balance: robustness of tip cell selection, migration and fusion in angiogenesis. *PLoS Comput. Biol.* **5,** e1000549 (2009).
45. Brockbank, E.C., Bridges, J., Marshall, C.J. & Sahai, E. Integrin beta1 is required for the invasive behaviour but not proliferation of squamous cell carcinoma cells *in vivo*. *Br. J. Cancer* **92,** 102–112 (2005).

nature cell biology

DOI: 10.1038/ncb2775

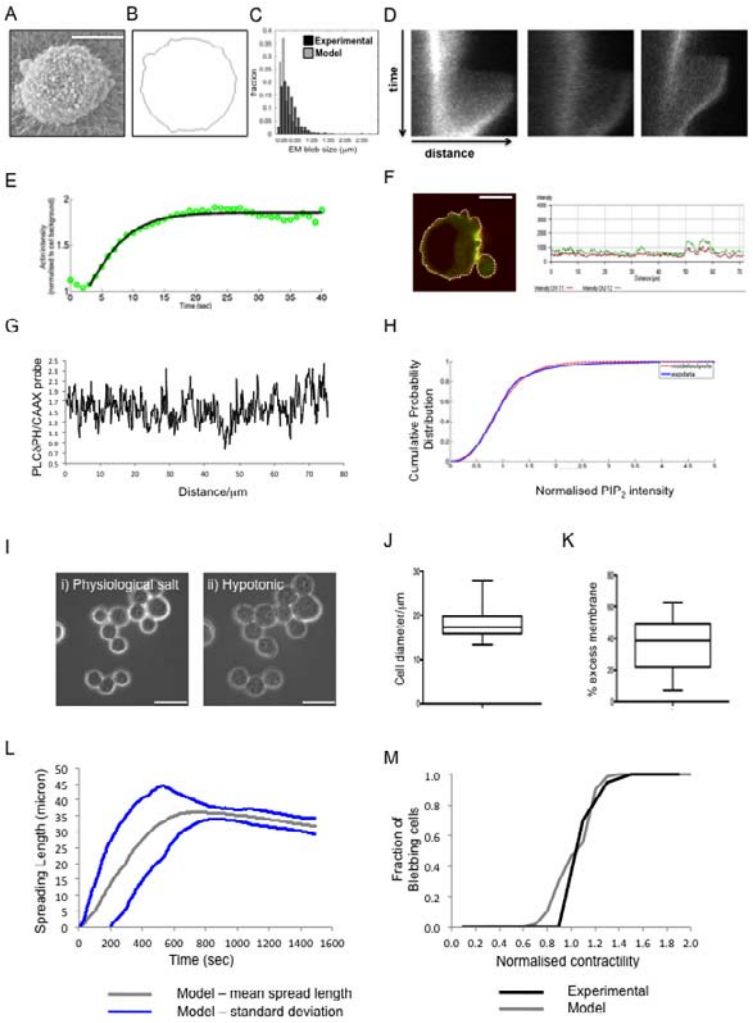

Figure S1 Model parameterisation measurements. Related to Figure 2. **A.** Measurement of small bleb sizes. Scanning electron microscopy image shows blebs on an A375P cell stimulated with 1% serum. Scale bar is 10 microns. **B.** Image shows a snap-shot of bleb sizes in model under equivalent level of contractility simulation. **C.** Histogram shows the similarity between the blebs sizes (μm) from the model (grey) and experimental measurements (black). 633 blebs measured from 18 cells. **D.** Actin re-accumulation at the bleb rim, and decay at bleb neck. Three representative examples of bleb kymographs generated from A375P cells expressing LifeAct-GFP and stimulated with 1% serum are shown. Distance (X) dimension is 4 microns and time (Y) dimension is 74 seconds. **E.** The LifeAct-GFP intensity was quantified from multiple blebs every second following bleb initiation. The normalised average values are shown in green circles and the fitted rate of actin polymerisation used in the model is shown in black. 8 blebs were measured. **F.** Fluctuations in PIP_2 distribution over the cell surface. Image shows merge of PLCδPH-GFP (labelling for PIP_2 - green), mRFP-CAAX (labelling for membrane - red) and line tracing of membrane. Plot shows PLCδPH-GFP (green) and mRFP-CAAX (red) intensity along the line traced in image. Scale bar is 10 microns **G.** Shows PLCδPH-GFP signal divided by mRFP-CAAX signal along the line traced in image **H.** Experimentally derived cumulative frequency of PIP_2 distribution (normalised values) in A375 cells is shown in blue. Distribution was derived only from the plasma membrane and not internal areas of the cell. 11 cells were analysed. The distribution used for the model is shown in red. The procedure is detailed in Sup. Note - *Proteins - PIP_2 Fluctuations and Inverse Transform Sampling*. **I.** Cell sizes and available membrane pool. Images show A375M2 in physiological salt (i) and after exposure severe hypotonic conditions leading to cell swelling and bursting (ii). Scale bar is 40μm. **J.** Average cell diameter calculated from images similar such as those in I(i). 36 cells were analysed. The whiskers indicate minimum and maximum values observed, line is the mean, the box is upper and lower quartiles of the data set. **K.** Average excess cell membrane is calculated in terms of percent increase in cell diameter, by comparison of the cell diameter in physiological salt compared to at the time of bursting due to hypotonic shock (The cells are assumed circular and the diameter measured accordingly from images in (i) & (ii)). 16 cells were analysed. The whiskers indicate minimum and maximum values observed, line is the mean, the box is upper and lower quartiles of the data set. **L.** Protrusion, spreading and blebbing dynamics for an unperturbed, non-polarised cell. Contact length between the cell and the surface as a function of time. Means (gray) and upper and lower standard deviation ranges (blue) are given. Each data point is average of 10 simulations. **M.** The fraction of blebbing cells among randomly taken snapshots throughout the simulation, as a function of overall myosin levels. The model values are given for all blebs recorded (gray). Black line represents experimental data for A375P cells. Cells were scored for the presence or absence of blebs and cortical pS19-MLC. The data were then 'binned' into groups based on contractile pS19-MLC values and the fraction of blebbing cells in each bin was calculated. Bins were 0-0.2, 0.2-0.4, 0.4-0.6, 0.6-0.8 and so on.

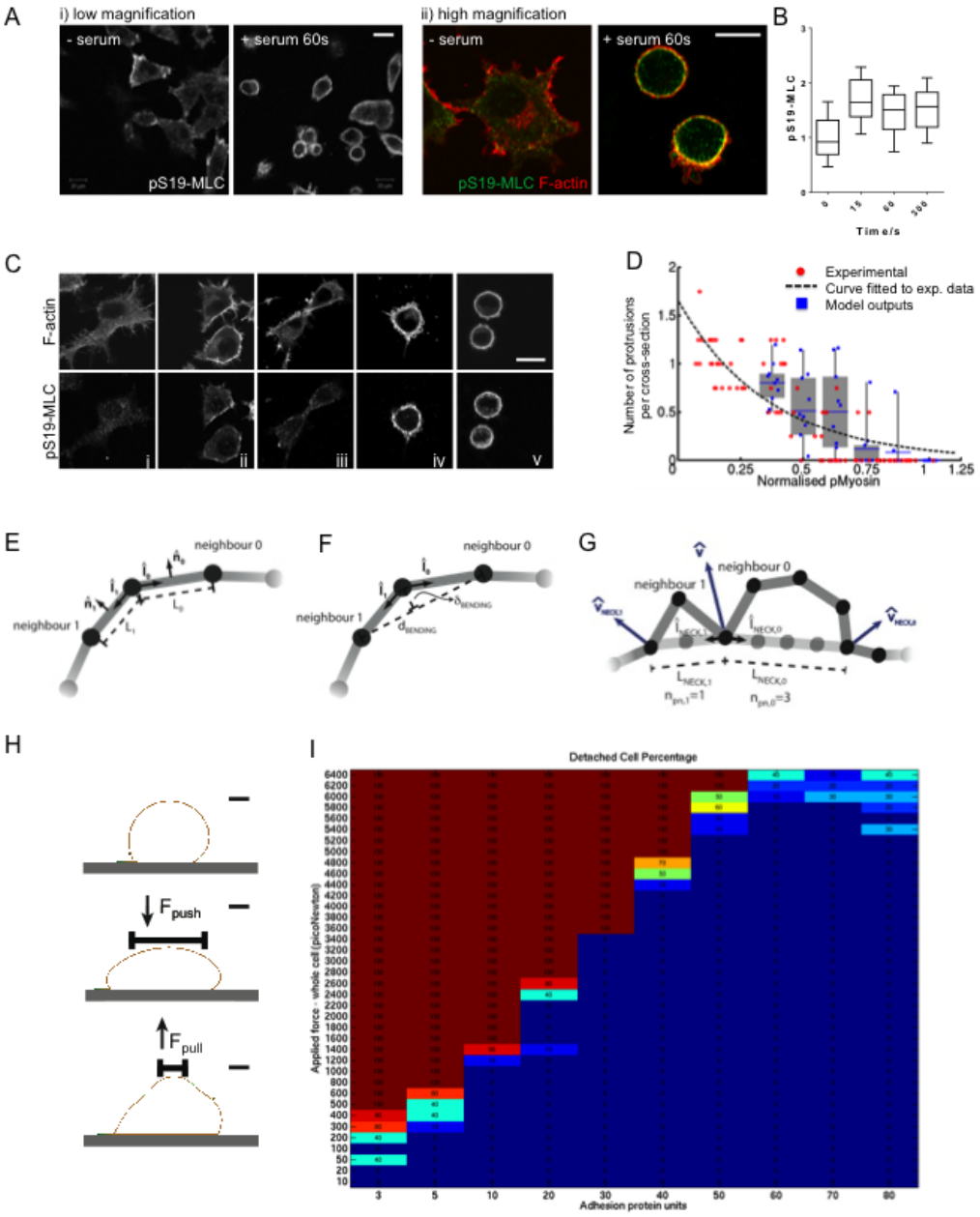

Figure S2 Cross talk between the regulatory mechanisms implemented in the model. Related to Figure2**. A.** Myosin response under serum stimulation. Images show pS19MLC staining of A375P cells either serum starved or 60s after the addition of 1% FCS. Scale bar is 20 microns. **B.** Quantification of pS19-MLC staining of A375P cells following the addition of 1% FCS. Box plots show the median, quartiles and 10%&90% values. (n=2 see Table S4 - Statistics Source Data). **C.** Cross-talk between protrusion initiation and contractility. Images show representative examples of A375P cells with varying levels of F-actin protrusions and pS19-MLC. Images i&ii are treated with 10μM Y27632, images iii-iv are serum starved and image v is stimulated with 1% serum. Scale bar is 20 microns. **D.** Quantification of the relationship between protrusions and pS19MLC is shown. Experimental data points are extracted from images such as those shown in 'A'. Cortical pS19-MLC fluorescence was quantified in each cell along with the average numbers of protrusions per cross-section of the cell. Four lines bisecting the cell were drawn at 45 degree angles. The presence or absence of a protrusion at each point where the line intersected the cell periphery was scored (four lines gave a total of eight intersections per cell). The number of protrusions was divided by 4. Model outputs are the number of spreading protrusions taken at random time intervals. 78 cells were analysed, each one shown in red. Each data point represents mean of 10 simulations (blue), upper and lower quartiles (boxes), and range (black line). **E-G.** Nomenclature for equations throughout the text. **E.** Length and direction notation for all agents of the model. **F.** Bending resistance calculation notation for all agents of the model. **G.** Notation for bleb neck force calculations, valid for bleb borders. **H.-I.** Atomic Force Microscopy mimicking simulations. Computational simulation of experiments with a matrix coated bead attached to the cantilever of an atomic force microscope. The bead is allowed to attach to the cell surface and the force required to pull the cantilever and bead off the cell is determined. Cell is allowed to spread on the surface. Initial spreading is followed by 50 seconds of pushing the cell to the surface with a force of 1 nN. Then the cell is pulled from the surface with variable forces. Scale bar is 5 microns. **I.** The percentage detachment of cells under variable adhesion levels, and pulling forces. The force values are evaluated for the 2D cell, a rough scaling to 3D would bring an approximate 70 fold increase to the forces required for detachment, bringing the detachment values within the ranges 20-2000 nN, reported for a variety of cell types [1, 2].

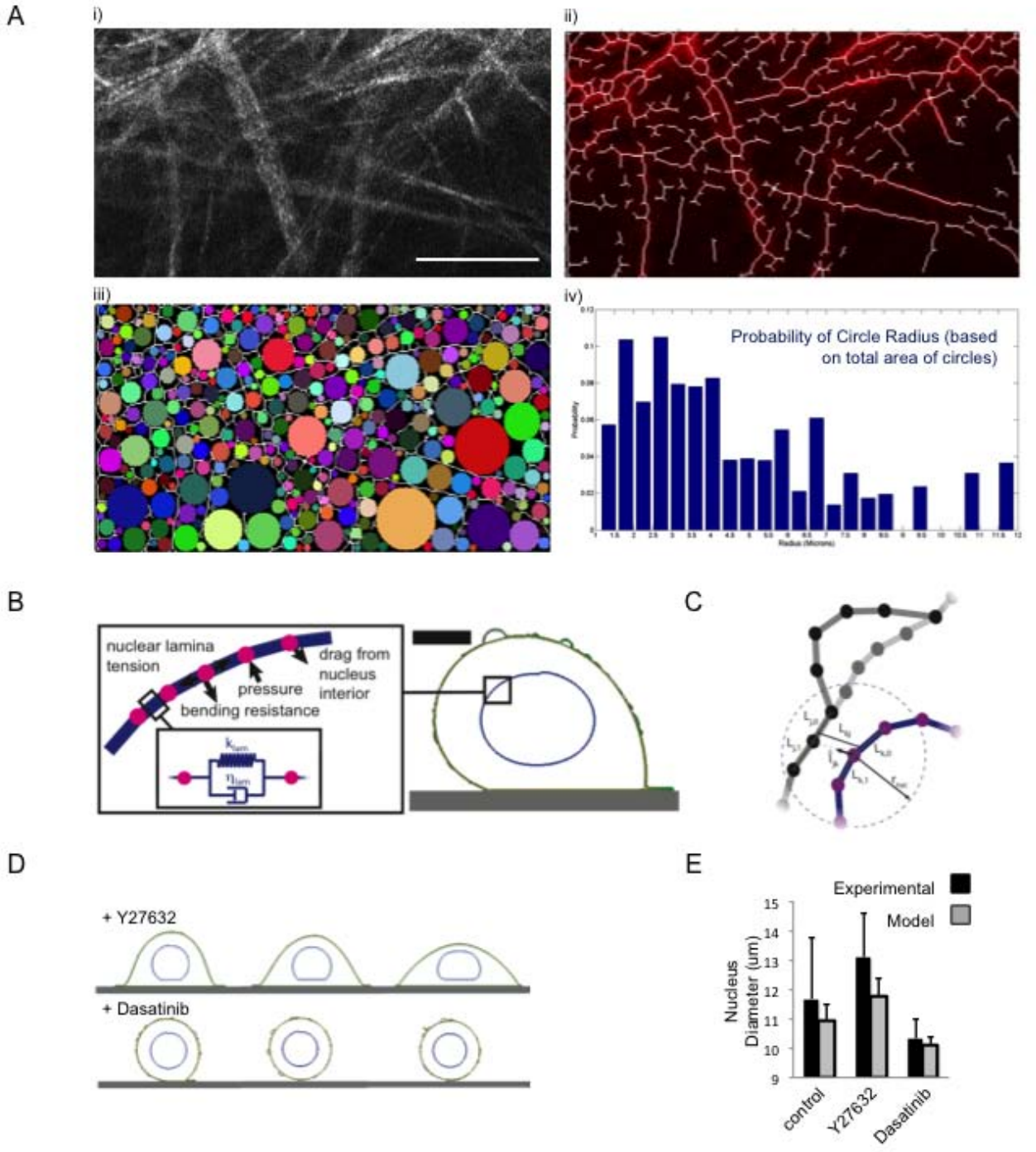

Figure S3 Quantification of collagen fibres surrounding melanoma and modelling of the nucleus. Related to Figure5. **A. i)** Image show collagen fibres around the margin of an A375 tumour imaged used second harmonic generation. Scale bar is 50 microns. **ii)** Automated filament tracing of collagen fibres. **iii)** Circles fitted into the gaps between collagen fibres are shown. **iv)** Histogram showing the frequency of different size radial spacing (diameter of fitted circles) between collagen fibres. B) Schematic representing the modelling of the cell nucleus. Each of the viscoelastic linkers represents a local patch of nuclear lamina. The scale bar is 5 microns in the model snapshot. C) The nomenclature used in nucleus related calculations. D) Model snapshots showing the spreading of cell, and deformation of nucleus, under Y27632 and Dasatinib treatment. E) The nuclear diameter size obtained from simulations such as in 'i &ii', and from 24,12, and 13 experimental cell measurements for Ctr, Y27632 and Dasatinib treated cells, respectively. Mean and standard deviation are shown (see Table S4 - Statistics Source Data for individual cell measurements).

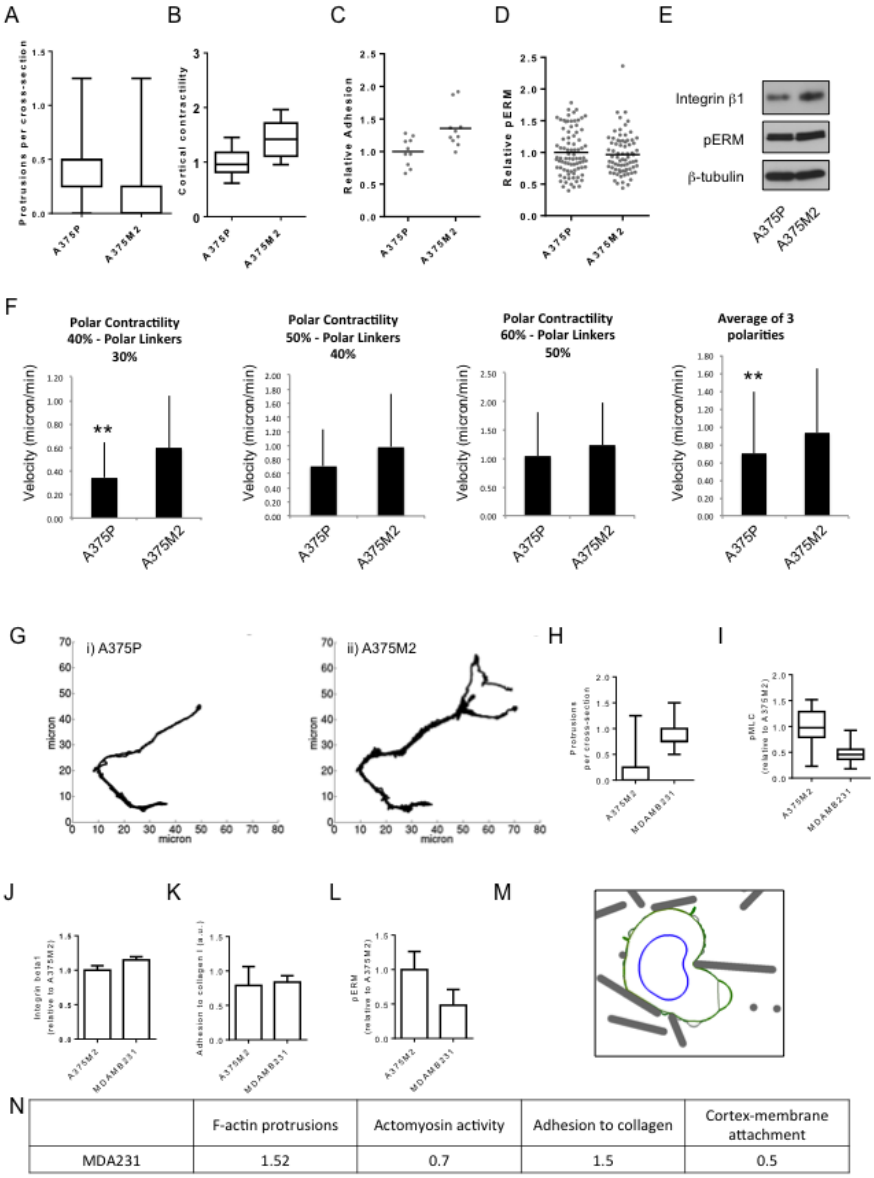

N

	F-actin protrusions	Actomyosin activity	Adhesion to collagen	Cortex-membrane attachment
MDA231	1.52	0.7	1.5	0.5

Figure S4 Comparison of A375P and A375M2 cells. Related to Figure 5. **A.** Difference in protrusion frequency between A375P and A375M2 cells. . Box plots show the median, quartiles and 10%&90% values. (n=2 see Table S4 - Statistics Source Data for individual cell measurements). **B.** Difference in cortical pS19-MLC between A375P and A375M2 cells. Box plots show the median, quartiles and 10%&90% values. (n=2 see Table S4 - Statistics Source Data). **C.** Adhesion to collagen I by A375P and A375M2 cells (n=10 from two independent experiments, all data points are shown together with the mean – see Table S4 - Statistics Source Data). **D.** Difference in pERM between A375P and A375M2 cells (two independent experiments, all data points are shown together with the mean – see Table S4 - Statistics Source Data). **E.** Representative western blots showing integrin β1, pERM and β-tubulin (loading control) levels in A375P and A375M2 cells. **F.** Velocities predicted by simulations, in vivo mimetic ECM. Polarities are indicated on each plot. n=30 independent simulations for each data point in each of the individual polarity plots, summing up to n=90 for each of A375P and A375M2 in polarity averages plot (One simulation is equivalent to 30 minutes of real time). 30 simulations of each data point are equally distributed among three randomly generated *in vivo mimetic* ECMs. Error bars indicate one standard deviation. ** indicates significant difference form M2 cells under same conditions (two tail t-test, $p<0.01$) **G.** Trajectories of simulations in one selected in vivo-mimetic ECM. 50% polar contractility and 40% reduced cortex-membrane linker polarity at the cell front is applied. **H.** Difference in protrusion frequency between MDAMB231 and A375M2 cells. Box plots show the median, quartiles and 10%&90% values. (A375M2 n=73, MDAMB231 n=20, see Table S4 - Statistics Source Data for individual cell measurements). **I.** Difference in cortical pS19-MLC between MDAMB231 and A375M2 cells. Box plots show the median, quartiles and 10%&90% values. (A375M2 n=22, MDAMB231 n=44, see Table S4 - Statistics Source Data for individual cell measurements). **J.** Difference in integrin β1 expression between A375P and A375M2 cells measured by immune-fluorescence. Box plots show the median, quartiles and 10%&90% values. (A375M2 n=22, MDAMB231 n=44, see Table S4 - Statistics Source Data for individual cell measurements). **K.** Adhesion to collagen I by MDAMB231 and A375M2 cells (average of four data points). **L.** Difference in pERM between MDAMB231 and A375M2 cells. Box plots show the median, quartiles and 10%&90% values. (A375M2 n=14, MDAMB231 n=42, see Table S4 - Statistics Source Data for individual cell measurements). **M.** Image showing model prediction of MDAMB231 migration in *in vivo* mimetic environment. **N.** Table shows input parameters used to generate the prediction shown in L. The values are normalised to A375P cells.

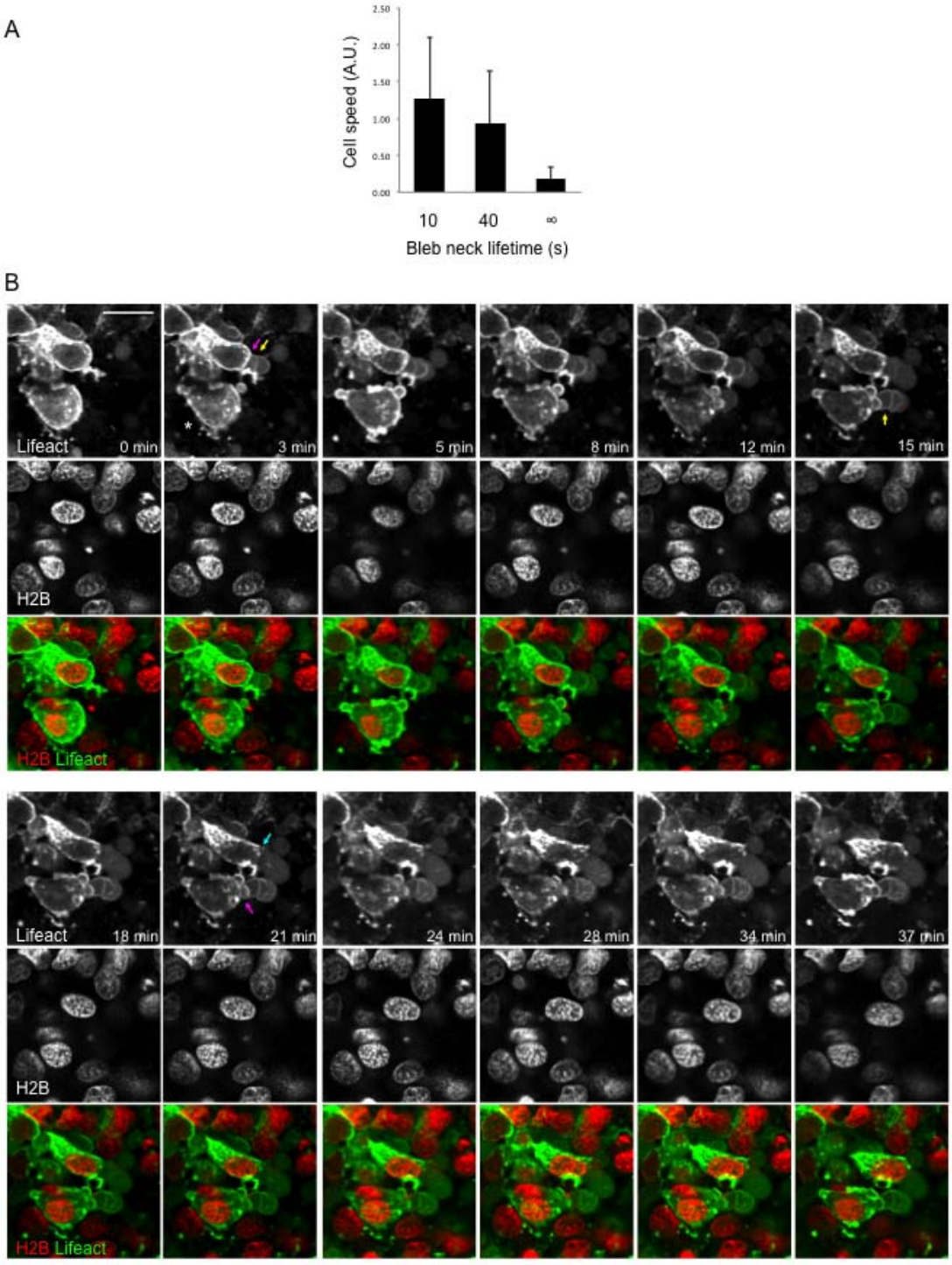

Figure S5 Bleb neck decay can limit cell migration. Related to Figure 5. **A.** Predicted cell migration depending on the rate of bleb neck depolymerisation. n=90 independent simulations for each data point, one simulation is equivalent to 30 minutes of real time. 90 simulations of each data point are equally distributed among three randomly generated *in vivo mimetic* ECMs, and three levels of cell polarity (polar contractility 40% and polar ERM 30%; polar contractility 50% and polar ERM 40%; polar contractility 60% and polar ERM 50%). Error bars indicate one standard deviation. **B.** Panels show LifeAct (green) and H2B (red) confocal sections of A375M2 cells *in vivo* at the indicated timepoints. Yellow arrow highlights bleb formation, magenta arrow shows bleb neck and cyan arrow indicates bleb neck de-polymerisation. Cell highlighted with * fails to depolymerise the bleb neck and does not translocate. Scale bar is 20μm.

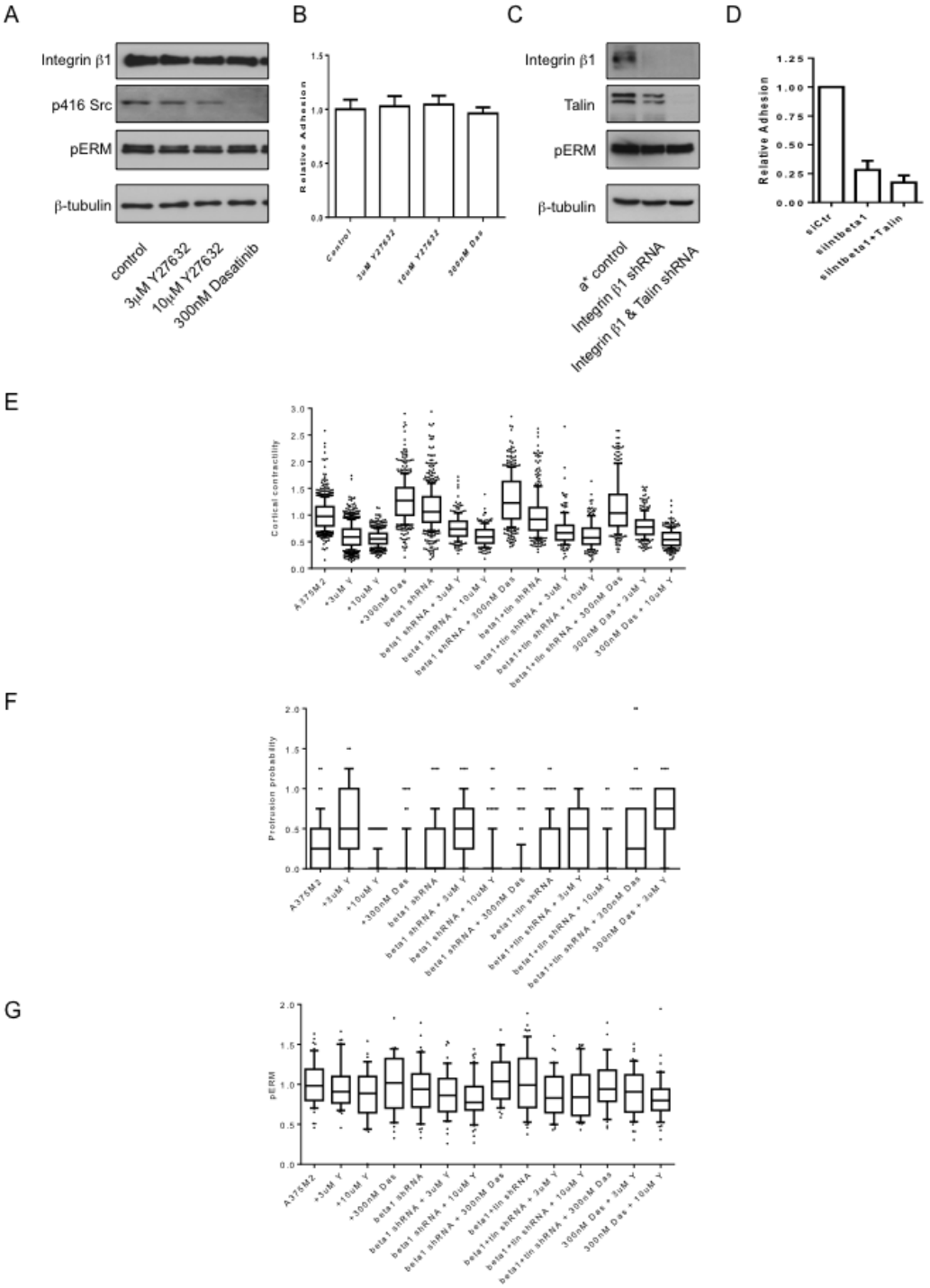

Figure S6 Characterisation of experimental perturbations *in vitro*. Related to Figure 6. **A.** Representative western blots showing integrin β1, p416-Src, pERM, and β-tubulin (loading control) levels in A375M2 cells following indicated drug treatments. **B.** Adhesion to collagen I by A375M2 cells following indicated drug treatment (8 data points and the mean from two independent experiments are shown – see Table S4 - Statistics Source Data file). **C.** Representative western blots showing integrin β1, Talin, pERM, and β-tubulin (loading control) levels in A375M2 cells following integrin β1 and integrin β1 + talin depletion. **D.** Adhesion to collagen I by A375M2 cells following integrin β1 and integrin β1 + talin depletion (n=5 independent experiments). **E.** Difference in cortical contractility as measured by pS19-MLC in A375M2 cells following the manipulations indicated. Box plots show the median, quartiles, 10%&90% values and outliers. (data pooled from 3 experiments a minimum of 175 cells analysed per data point, see Table S4 - Statistics Source Data for individual cell measurements). **F.** Difference in protrusion probability in A375M2 cells following the manipulations indicated. Box plots show the median, quartiles, 10%&90% values and outliers. (data pooled from 2 experiments a minimum of 68 cells analysed per data point, see Table S4 - Statistics Source Data for individual cell measurements). **G.** Difference in pERM between in A375M2 cells following the manipulations indicated. Box plots show the median, quartiles, 10%&90% values and outliers. (data pooled from 2 experiments a minimum of 40 cells analysed per data point, see Table S4 - Statistics Source Data for individual cell measurements).

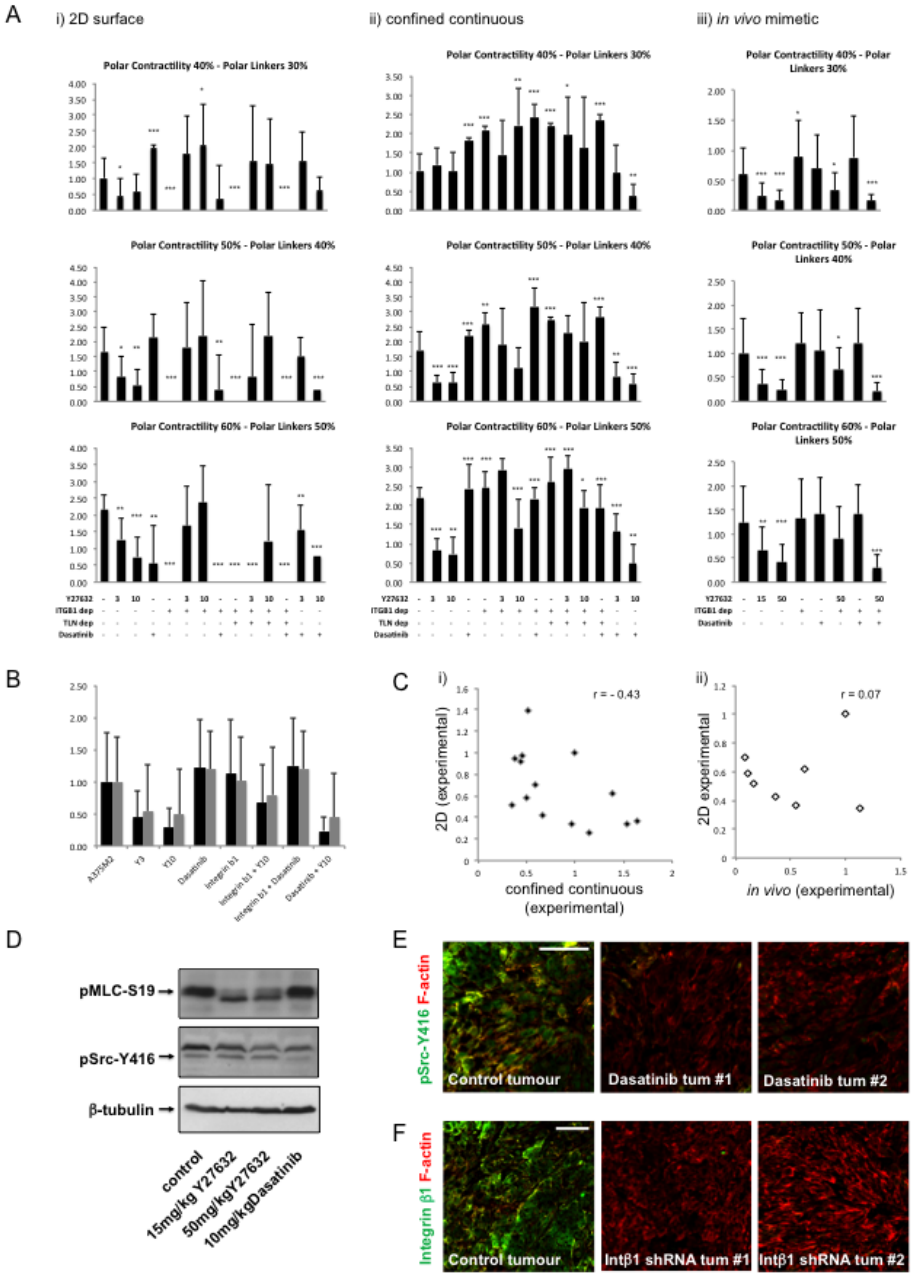

Figure S7 Comparison of model predictions and experimental motility measurements *in vivo*. Related to Figure 6. **A.** Results of simulations for perturbations with differing levels of asymmetry are shown. i) 2D surface predictions ii) confined continuous environment predictions For i and ii, n=10 for each data point, (summing up to n=30 in Figure6Bi&ii) iii) *in vivo* mimetic environment. n=30 for each data point (summing up to n=90 in Figure6Bv). The sample points are equally distributed among three randomly generated *in vivo* mimetic ECMs. For panels i, ii & iii, one standard deviation is shown as error bars. Significant differences from control under the same conditions are marked (two-tail t-test, * indicates p value<0.05, ** p value < 0.01, *** pvalue <0.001). **B.** Comparison of two different methods for predicting the effect of experimental perturbations in vivo. Black bars show the predicted average speed of cells following the indicated perturbations. Grey bars show the proportion of time cells exhibit a velocity above 0.5μm/min, which corresponds to the speed of cell migration that can unambiguously be detected using in vivo imaging. Values normalised to control. n=90 for each data point, the data is extracted from the simulations in panel Aiii. Error bars indicate one standard deviation. **C.** Plots show the correlation of relative changes in migration on 2D surfaces (experimentally deterimined) and changes in migration in confined continuous environments (panel i) and *in vivo* (panel ii). Pearson co-efficients are indicated. **D.** Western blots show pS19-MLC, pY416-Src (lower band marked with arrow), and β-tubulin (loading control) levels in tumour lysates in mice treated with the indicated doses of Y27632 or Dasatinib. **E.** Immuno-staining of tumours in control and Dasatinib-treated mice (10mg/kg) showing pY416-Src in green and F-actin in red. Scale bar is 50μm. **F.** Immuno-staining of control and integrin β1 shRNA tumours showing human integrin β1 in green and F-actin in red. Scale bar is 50μm.

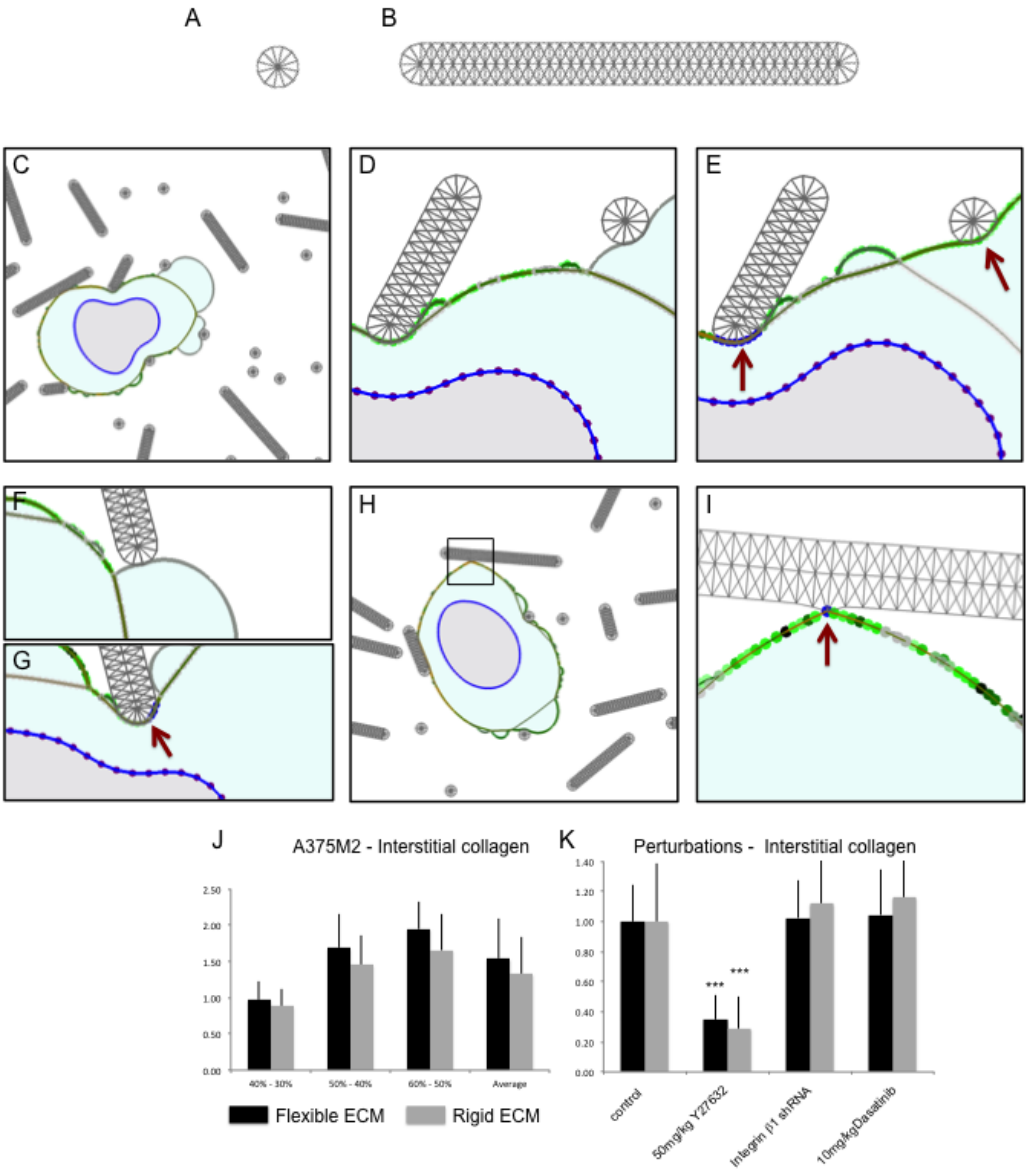

Figure S8 Modelling and predictions on deformable extracellular matrix filaments. **A.-B.** The spring networks used to define deformable ECM filaments. **C.-I.** Model snapshots demonstrating the deformations on the fibres. **C.** A375M2 cell within in vivo mimetic environment. **D.** An expanding bleb that cannot deform the matrix filament. **E.** The retracting blebs can apply enough pressure forces to deform the filaments, as well as the non-blebbing cell surface (red arrows). **F.** Close snapshot of an expanding bleb in contact with ECM. **G.** Cell body can apply lateral forces to filaments to cause deformations. **H.** In addition to pressure forces at the cell front and sides, the cell can apply pulling forces at the cell rear, and deform the filaments. **I.** Close snapshot of inset marked in H. **J.** Predicted melanoma velocities at changing polarities, in an *in vivo* mimetic environment with rigid (grey) and flexible (black) filaments. For each of the polarities, n=15 for flexible ECM, and n=20 for rigid ECM, summing up to n=45 for the average values data point for flexible ECM, and n=60 for rigid ECM. There is no significant difference in between two setups (two tail t-test, all p-values >0.05). The simulations are distributed amongst two randomly generated *in vivo* mimetic ECMs. Error bars indicate one standard deviation. **K.** Changes in cell motility upon interventions, in an *in vivo* mimetic environment with rigid (grey) and flexible (black) filaments. Only myosin depletion, via inhibition of ROCK kinases using Y27632, has a significant difference from control in both setups (two tail t-test, p-value < 1E-12, all non-significant cases, p-value > 0.05). For flexible ECM, the independent simulation numbers are n=45, 60, 40, 20 for control, Y27632, integrin b1, and dasatinib treatments, respectively. For rigid ECM, n=60 for all data points. The independent simulations are distributed amongst three levels of polarity (same as indicated in panel J), and two randomly generated *in vivo* mimetic ECMs. Error bars indicate one standard deviation.

Supp. Fig6a

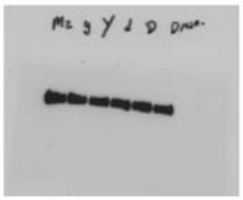

Integrinb1

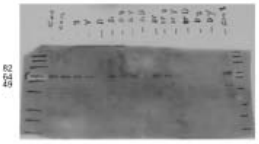

pY416-Src

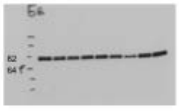

pERM

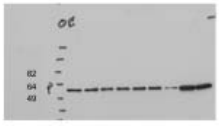

B-tubulin

Supp. Fig6c

Integrinb1

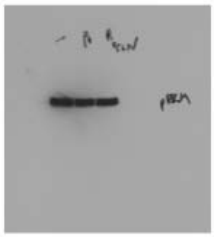

pERM

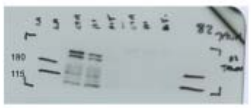

Talin

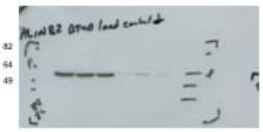

B-tubulin

References

1. Moore, S., Roca-Cusachs, P. & Sheetz, M. Stretchy proteins on stretchy substrates: the important elements of integrin-mediated rigidity sensing. *Dev. Cell* **19,**194-206 (2010).
2. Friedrichs, J., Manninen, A., Muller, D. & Helenius, J. Galectin-3 regulates Integrinβ 1-mediated adhesion to collagen-I and -IV. *J. Biol. Chem.* **283,** 32264–32272 (2008).
3. Tinevez, J-Y. *et al.* Role of cortical tension in bleb growth. *Proc. Natl Acad. Sci. USA* **106,** 18581–18586 (2009).
4. Coskun, H., Li, Y. & Mackey, M. Ameboid cell motility: a model and inverse problem, with an application to live cell imaging data. *J. Theoret. Biol.* **244,** 169-179 (2007).
5. Charras, G., Coughlin, M., Mitchinson, T. & Mahadevan, L. Life and times of a cellular bleb. Biophys. J. **94,** 1836-1853 (2008).
5 Yumura, S. Myosin II dynamics and cortical flow during contractile ring formation in Dictyostelium cells. *J. Cell Biol.* **154,** 137-145 (2001).
6. Raucher, D. Characteristics of a membrane reservoir buffering membrane tension. *Biophys. J.* **77,** 1992-2002 (1999).
Boal, D. Mechanics of the Cell (Cambridge Univ. Press, 2001).
7. Guilak, F., Tedrow, J. & Burgkart, R. Viscoelastic properties of the cell nucleus. *Biochem. Biophys. Res. Commun.* **269,** 781–786 (2000).
8. Caille, N., Thoumine, O., Tardy, Y. & Meister, J-J. Contribution of the nucleus to the mechanical properties of endothelial cells. *J. Biomech.* **35,** 177–187 (2002).
9. Charras, G., Hu, C-K., Coughlin, M. & Mitchison, T. Reassembly of contractile actin cortex in cell blebs. *J. Cell Biol.* **175,** 477-490 (2006).
10. Cojoc, D. et al. Properties of the force exerted by filopodia and lamellipodia and the involvement of cytoskeletal components. *PloS ONE* **2**, e1072, (2007).
10. Mogilner, A. & Rubinstein, B. The physics of filopodial protrusion. *Biophys. J.* **89,** 782-795 (2005).
11. Raucher, D. & Sheetz, M.P. Cell spreading and lamellipodial extension rate is regulated by membrane tension. *J. Cell Biol.* **148,** 127-136 (2000).
12. Mallavarapu, A. & Mitchison, T. Regulated actin cytoskeleton assembly at filopodium tips controls their extension and retraction. *J. Cell Biol.* **146,** 1097-1106 (1999).
13. Bell, G.I. Models for the specic adhesion of cells to cells. *Science* **200,** 618-627 (1978).
14. Paszek, M. et al. Tensional homeostasis and the malignant phenotype. *Cancer Cell* **8,** 241-254 (2005).
14. Levental, K. et al. Matrix crosslinking forces tumor progression by enhancing integrin signaling. *Cell* **139,** 891-906 (2009).

Supplementary Video Legends

Supplementary Video 1 Model output demonstrating the spreading of a serum starved cell on a non-confined surface, followed by serum stimulation, rounding up and blebbing (related to Figure 2c). Serum starved cell spreading on a continuous non-confined surface. Cell initiated with contractility = 0.8, and serum stimulated = 1.6 contractility at 400 seconds. Cell membrane is represented in grey, actin cortex in green and myosin in red. Scale bar is 5 μm.

Supplementary Video 2 Phase contrast movie and fluorescence movie of MLC-GFP of a serum starved cell on a collagen matrix, followed by serum stimulation at 180 sec (related to Figure 2d). Section i) Phase contrast movie of a serum starved cell on a collagen matrix. 1% FCS is added at frame 45. Frames are 4s apart. Section ii) Fluorescence movie of MLC-GFP of a serum starved cell on a collagen matrix. 1% FCS is added at frame 45. Frames are 4s apart.

Supplementary Video 3 Computational simulations of cell migration on 2D surface (related to Figure 3c). Section i) Simulation of a cell moving on a continuous non-confined surface. Cell contractility = 1.0, adhesion = 3.0, rearward asymmetries in contractility and cortex-membrane linkage are 30% and 20%, respectively. Cell membrane is represented in grey, actin cortex in green and myosin in red. The colour intensities, scaled to protein concentrations are overlaid, for example generating colour orange for high myosin-high actin regions. Arrows indicate the forces exerted on the matrix (red indicates high force, green intermediate, and blue low force). The logarithmic scale for the forces exerted is given on the video, in the range 1E-3 pN to 1E3 pN. Section ii) A zoomed in view of the cell protrusion is shown. Section iii) A zoomed in view of the cell rear is shown. Scale bar is 5 μm.

Supplementary Video 4 Computational simulations of cell migration in confined continuous environment (related to Figure 3c). Simulation of a cell moving in a continuous confined environment. The confinement size is 10μm. Cell contractility = 1.0, adhesion = 3.0, rearward asymmetries in contractility and cortex-membrane linkage are 30% and 20%, respectively. Colours are as in supplementary movie 3. Scale bar is 5 μm. The cortex inside the actin polymerisation based protrusions decay in time, and the density of these structures are colour coded in the movie, leading to greyish colours on these linkers close to the complete disassembly, which should not be confused with the colour coding of the cell membrane, which lies outside the actin cortex.

Supplementary Video 5: Computational simulations of cell migration in confined continuous environment (related to Figure 3c). Simulation of a cell moving in a continuous confined environment. The confinement size is 10μm. Cell contractility = 1.5, adhesion = 3.0, rearward asymmetries in contractility and cortex-membrane linkage are 30% and 20%, respectively. Colours are as in supplementary movie 3. Scale bar is 5 μm. The cortex at plasma membrane bleb necks decay in time, and the density of these structures are colour coded in the movie, leading to greyish colours on these linkers close to the complete disassembly, which should not be confused with the colour coding of the cell membrane, which lies outside the actin cortex.

Supplementary Video 6 Computational simulations of cell migration in confined discontinuous environment (related to Figure 3c). Simulation of a cell moving in a discontinuous confined environment. Vertical confinement is 10μm and lateral gaps are 4.3μm. Cell contractility = 1.5, adhesion = 0, rearward asymmetries in contractility and cortex-membrane linkage are 30% and 20%, respectively. Colours are as in supplementary movie 3. The cortex at plasma membrane bleb necks decay in time, and the density of these structures are colour coded in the movie, leading to greyish colours on these linkers close to the complete disassembly, which should not be confused with the colour coding of the cell membrane, which lies outside the actin cortex.

Supplementary Video 7 A375M2 cell in the *in vivo* mimetic environment (related to Figure 5B). Cell has 50% increased contractility at the cell rear and 40% reduced cortex membrane linkers at the front. Cell moves using blebs to propel the plasma membrane forward. Cell membrane is represented in grey, actin cortex in green and myosin in red. The cortex at plasma membrane bleb necks decay in time, and the density of these structures are colour coded in the movie, leading to greyish colours on these linkers close to the complete disassembly, which should not be confused with the colour coding of the cell membrane, which lies outside the actin cortex.

Supplementary Video 8 Moving A375M2 cell *in vivo* (related to Figure 5Biii). Intravital imaging showing A375M2 cell moving at the tumour margin: green shows LifeAct and red shows Histone H2B. Movie spans 24 minutes.

Supplementary Video 9 Moving A375M2 cells *in vivo* (related to Supplementary Figure5. **A.** Intravital imaging showing A375M2 cell moving at the tumour margin: green shows LifeAct and red shows Histone H2B. Movie spans 37 minutes.

Supplementary Video 10 MDAMB231 cell in the *in vivo* mimetic environment (related to Figure5A). Cell has 50% increased contractility at the cell rear and 40% reduced cortex membrane linkers at the front. Cell moves using blebs to propel the plasma membrane forward. Cell membrane is represented in grey, actin cortex in green and myosin in red. Scale bar is 5 mm.

Supplementary Video 11 Moving MDAMB231 cell *in vivo* (related to Figure5D). Intravital imaging showing A375M2 cell moving at the tumour margin: green shows LifeAct and magenta shows collagen second harmonic signal. Movie spans 10 minutes.

Supplementary Video 12 Blebbing migration in a primary human cancer biopsy (related to Figure5E). Timelapse imaging shows migration of cell from a primary human oral squamous cell carcinoma moving between two planar collagen-rich matrices. Movie spans 120 minutes.

Supplementary Video 13 Integrin β1 depleted A375M2 cell *in vivo* (related to Figure6E). Intravital imaging showing integrin β1 depleted A375M2 cell moving: green shows LifeAct-GFP. Movie spans 30 minutes. Details of blebbing events are marked in Figure6E.

SUPPLEMENTARY NOTE- Matrix geometry determines optimal cancer cell migration strategy and modulates response to interventions.

Melda Tozluoğlu[1], Alexander L. Tournier[1], Robert P. Jenkins[2], Steven Hooper[2], Paul A. Bates[1] and Erik Sahai[2]

The Model

The Actomyosin Cortex and the Membrane

The tension at the cell surface is linked to the viscoelastic actin network, the tension generated by myosin motors, and the tension in the membrane. The viscoelastic response of the actin cortex is modelled with a Kelvin-Voigt body (Figure1). Myosin generated contractility is modelled with a spring of zero ideal length between the agents. The membrane spring models the resistance of the membrane. The forces acting on each agent due to actomyosin cortex and membrane are given as:

$$\mathbf{F_{COR}} = \sum_{i=1:2} \left(k_{COR} \left(L_i - L_i^0 \right) - \eta_{\mathrm{COR}} \hat{\mathbf{l}}_i . \left(\mathbf{v} - \mathbf{v}_i \right) + k_{MYO} L_i + k_{MEM} L_i \right) \hat{\mathbf{l}}_i + \mathbf{F_{BEN}} \ , \qquad \text{S1}$$

where k_j is the spring constant of j (cortex, myosin or membrane), and η_{COR} is the cortex drag coefficient. Summations are over the neighbours i of the agent. L_i is the current length of the linker attaching the agent to its neighbour i. $\hat{\mathbf{l}}_i$ is the unit vector in the direction of its neighbour i (FigureS2E). $\mathbf{v}$ is the velocity of the current agent and $\mathbf{v}_i$ is the velocity of the neighbour i. $\mathbf{F_{BEN}}$ is the force due to bending resistance of the cortex and the membrane.

The physical properties of the actin cortex and the cytoskeleton at any given point on the cell surface are dependent on the density of the cortex, as a fraction of normal cortex density, and the local protein concentrations. The strength of k_{COR} and η_{COR} are dependent on the cortex fraction of the linker (Equation S2-3), such that

$$k_{COR} = k_{COR}^0 f_{COR} \ , \qquad \text{S2}$$

$$\eta_{COR} = \eta_{COR}^0 f_{COR} \ . \qquad \text{S3}$$

Here, f_{COR} is the current cortex density as a fraction of normal cortex density. Ideal length, L_i^0, of the actin springs is regulated by the actin renewal rate (see *Proteins – Actin Cortex and Myosin*). Stiffness of the myosin spring, k_{MYO}, is dependent on the myosin concentrations at the linked agents (Equation S4) via,

$$k_{MYO} = k_{MYO}^0 c_{MYO} \ . \qquad \text{S4}$$

c_{MYO} is the average myosin concentration in the linked agents, where normal is 1. The strength of the membrane spring is dependent on the total surface of the cell [1] (see below). $\mathbf{F_{BEN}}$ Is the force due to bending resistance of the cortex and the

membrane, the bending rigidity is also dependent on the cortex fraction, and the force is calculated from,

$$B_{COR} = \left(f_{COR} - f_{COR}^{BLEB}\right)\frac{B_{COR}^{0} - B_{COR}^{BLEB}}{1 - f_{COR}^{BLEB}} + B_{COR}^{BLEB} \quad . \qquad \text{S5}$$

B_{COR}^{BLEB} is the bending rigidity of a bleb, f_{COR}^{BLEB} is the residual cortex fraction in a bleb, and B_{COR}^{0} is the normal bending rigidity (see *Bending Resistance* and FigureS2F) [2].

Cells have excess membrane [1], and the membrane does not contribute to tension until the membrane pool of the cell is depleted. On the other hand, when the pool is depleted, the lipid bilayer has a very limited stretching capacity, 4%, beyond which it tears at points of tension [3]. We modelled this behaviour with a total cell surface dependent elastic response. The relation between k_{MEM}, spring constant of the membrane, and S_{CELL}, the total cell surface, is given in equation S6. The relationship between S_{CELL}^{POOL}, the excess membrane pool percentage; Δ_{TR}, the stretch limit of the lipid bilayer before tearing; k_{TR}, the spring constant at the moment of tearing, and δ^{MEM} the step function are given in equation S6. k_{TR} is calculated from [3] with the same methodology used for k_{MYO} (see *Calculated Parameters*). The size of the membrane pool is measured (FigureS1J-K); we used a pool to support a 40% increase in the cell diameter. The relation is given as:

$$k_{MEM} = \frac{k_{TR}}{S_{CELL}^{POOL}\Delta_{TR}}\left(S_{CELL} - S_{CELL}^{POOL}\right)\delta^{MEM} \quad ,with \qquad \text{S6}$$

$$\delta^{MEM} = \begin{cases} 0 & if \quad S_{CELL} < S_{CELL}^{POOL} \\ 1 & if \quad S_{CELL} > S_{CELL}^{POOL} \end{cases} \quad .$$

The exact shape of the function in equation S6 is not of significance, as long as the tension generated by the membrane increases dramatically, reaching the tearing tension at the tearing strain limit [4].

Bending Resistance

The aforementioned bending resistance is calculated as

$$\mathbf{F_{BEN}} = B_{BEN}\frac{\delta_{BEN}}{d_{BEN}^2}\frac{\sum_i \hat{\mathbf{l}}_i}{\left\|\sum_i \hat{\mathbf{l}}_i\right\|} \quad \text{S7}$$

The bending modulus, B_{COR}, is dependent on the cortex fraction of the region (Equation S7). The distance between the two neighbours of the agents is d_{BEN}, and the deflection of the agent from the base linking its neighbours is δ_{BEN} (FigureS2F).

Internal Cell Body

The cell has a resting internal pressure P_{CELL}^0. Deviations from the resting volume, area in our case, A_{CELL}^0, change the internal pressure via the cell bulk modulus, K_{CELL}, according to

$$P_{CELL} = P_{CELL}^0 + K_{CELL}\ln\left(\frac{A_{CELL}^0}{A_{CELL}}\right). \quad \text{S8}$$

Forces acting on each agent due to internal pressure are given in equation S9, where P_{CELL} is the current pressure of the cell, $\hat{\mathbf{n}}_i$ is the normal unit vector to $\hat{\mathbf{l}}_i$ direction of neighbour i. L_i is the length associated with the agent on the side of neighbour i (FigureS2E) and the cell cross-section in the 2D model is defined with a width, w_{MODEL}, which gives the pressure forces as:

$$\mathbf{F_P} = w_{\text{model}}\sum_i P_{CELL}\frac{L_i}{2}\hat{\mathbf{n}}_i. \quad \text{S9}$$

The cell cytoskeleton, defined as the cytoplasm and the internal actin mesh of the cell body, also has a viscous resistance to changes in cell shape [5] with drag coefficient η_{CELL}, the internal cell body force, $\mathbf{F_{CIN}}$, is calculated from

$$\mathbf{F_{CIN}} = \eta_{CELL}\mathbf{v}\sum_i \frac{L_i}{2}. \quad \text{S10}$$

The cell size and velocity are at the low Reynolds number range; we can assume an over-damped system, where the forces acting on each agent will be equilibrated by the dissipative force from the drag of the cell cortex and internal cell body. Therefore, the velocity of each agent can be calculated by the system of equations constructed from equation S1 written for each agent, such that

$$\eta_{CELL}\mathbf{v}\sum_i \frac{L_i}{2} + \sum_i \left(\eta_{\mathrm{COR}}\hat{\mathbf{l}}_i.\left(\mathbf{v}-\mathbf{v}_i\right)\hat{\mathbf{l}}_i\right) = \sum_i \left(k_{COR}\left(L_i - L_i^0\right) + k_{MYO}L_i + k_{MEM}L_i\right)\hat{\mathbf{l}}_i + \mathbf{F_P} + \mathbf{F_{BEN}} + \mathbf{F_{TIP}} + \mathbf{F_{NECK}} \ . \quad \text{S11}$$

Here, $\mathbf{F}_{\mathrm{NECK}}$ is the force acting on an agent at the bleb neck, due to the residual bleb neck cortex (Equation S18), and $\mathbf{F}_{\mathrm{TIP}}$ is the force acting on an actin polymerisation based protrusion tip, due to the polymerisation events. These forces are explained in detail in corresponding sections below. The drag coefficient is lower within an expanding bleb, and is restored with actin accumulation in the bleb, i.e. for any given bleb, the drag coefficient is a function of the average cortex fraction, $\langle f_{COR} \rangle$, of the bleb, and the normal drag coefficient η^0_{CELL} (Equation S12):

$$\eta_{CELL} = \eta^0_{CELL}\langle f_{COR}\rangle \ . \quad \text{S12}$$

Nucleus

The nucleus is modelled very similar to the whole cell itself. The nuclear lamina is formed by a set of nucleus agents, and the viscoelastic linkers in between. Differing from the modelling of the cell surface, the nuclear lamina does not have myosin driven contractility. The deformations of the nucleus are limited compared to the cell body, and the nucleus shape changes are not likely to deplete nuclear membrane, thus membrane tension acting on the nuclear lamina is not implemented explicitly in the model. Bending resistance forces acting on nucleus agents are calculated with the same approach described for agents of the cell cortex (See *Bending Resistance*). The nucleus body has the same viscoelastic responses as the internal cell cytoskeleton and cytoplasm (FigureS3B).

The forces acting on each of the nucleus agents due to the stiffness of nuclear lamina then become:

$$\boldsymbol{F}_{LAM} = \sum_{i=0:1}\left(k_{lam}(L_i - L_i^0) - \eta_{lam}\hat{l}_i \,.\, (\boldsymbol{v} - \boldsymbol{v_i})\right)\hat{l}_i \ . \quad \text{S13}$$

Here, k_{lam} is the spring constant for nuclear lamina, L_i is the distance toward neighbour i of the nucleus agent, L_i^0 is the ideal length of the link between the agent and its neighbour, η_{lam} is the viscous damping coefficient of nuclear lamina, $\mathbf{v}$ is the velocity of the nucleus agent, $\mathbf{v}_i$ is the velocity of neighbour i, and finally, $\hat{\boldsymbol{l}}_{\boldsymbol{i}}$ is the unit vector in the direction of neighbour i.

Similar to the cell cytoskeleton and cytoplasm, the nucleus has an ideal area, $\mathbf{A}^0_{\mathbf{nuc}}$,

and deviations from this ideal size causes changes in the internal pressure of nucleus, in a relation analogous to Equation S8:

$$P_{nuc} = P^0_{nuc} + K_{nuc} ln\left(\frac{A^0_{nuc}}{A_{nuc}}\right). \quad \text{S14}$$

Here, P^0_{nuc} is the hydrostatic pressure difference between the nucleus and the internal cell body, and its value is set to zero. K_{nuc} is the bulk modulus of the nucleus, which, is parameterised scaled to the bulk modulus of the cell, K_{cyt}, based on experimental data.

Our experimental observations point out that the movements of the nucleus correlate with the movement of the cell centre of mass. The contribution of the cell movement to movement of the nucleus is incorporated into the model by using the relative velocity of the nucleus agents with respect to the cell centre of mass velocity, $\mathbf{v}_{CELL}$, during the calculation of the viscous drag felt by nucleus agents. In a relation analogous to Equation S10, the force calculation becomes:

$$\boldsymbol{F}_{CIN} = \eta_{nuc}(\boldsymbol{v} - \boldsymbol{v}_{CELL}) \sum_{i=0:1} \frac{L_i}{2}. \quad \text{S15}$$

Here, $\mathbf{v}$ is the velocity of the nucleus agent, and $\boldsymbol{\eta}_{nuc}$ the viscous damping coefficient, representing the drag from both the interior of the nucleus, and the surrounding cytoskeleton. For the interactions with the cortex, when the cell is under confinement and the nucleus is packed against a part of the cell cortex, the compression of cytoskeleton in between the nucleus and the cortex is reflected on each of the nucleus and cortex agents:

$$\boldsymbol{F}_{NCP} = w_{model} \hat{l}_{kj} K_{cyt}\ ln\left(\frac{r_{nuc}}{L_{kj}}\right) \times \frac{1}{2} \sum_{i=0:1} \frac{L_{ji}}{2} + \frac{L_{ki}}{2}. \quad \text{S16}$$

The terms used in above equations are represented in FigureS3C. The force term $\mathbf{F}_{NCP}$ represents the nucleus–cortex packing. Here, r_{nuc} is the cut-off distance under which the cortex begins to have an effect on the shape and position of the nucleus - obtained from experimental observations. The subscript k indicates the nucleus agent of interest; subscript j indicates the cortex agent. $\hat{l}_{kj}$ is the unit vector in the direction from the nucleus agent k to cortex agent j, and L_{jk} is the distance between the cortex agent j and the nucleus agent k. L_{ji} are the distances between the cortex agent j and its neighbours, similarly, L_{ki} are the distances between the nucleus agent k, and its neighbours. The pressure accumulated in the segment due to compression

is calculated analogous to cell internal pressure calculation, with K_{cyt} the bulk modulus of the internal cell body, and w_{model} is the defined cross-section width of the 2D model cell. The force calculated above is applied to the cortex agent j and a force of equal magnitude and opposite direction is applied to the nucleus agent k. For every nucleus agent k, the force calculation is repeated for all cortex agents that are within r_{nuc}. Bleb neck agents are included in this calculation, while blebbing membrane agents are not. Simulations including a nucleus were run with the improved Bleb Neck modelling described on page 9.

The structural properties of both the nucleus and the nucleoskeleton are different than that of the bulk cell body and the F-actin cortex: the nucleus is stiffer and more viscous than the cytoskeleton and the F-actin cortex [6]. The bulk behaviour of the nucleus is viscoelastic, similar to the rest of the cell, but it is three to ten times stiffer than, and approximately twice as viscous as, the whole cell [7, 8]. All the parameters of the nucleus are scaled from the properties of cell F-actin cortex and the cytoskeleton. The nucleus is set to be three times stiffer than, and twice as viscous as, the cell cortex and internal cell body, setting k_{lam} at 720pN μN^{-1}, η_{lam} at $18000 pN\ s\ \mu N^{-1}$, B_{lam} at $0.645 pN\ \mu N$, η_{nuc} at 200pN s μN^{-2}, and K_{nuc} at 6750 Pa. Although this scaling is reported in the literature, the parameters are also tested with a cell spreading analysis. Spreading cells obtain a pancake shape, their nucleus being pushed against the surface and being deformed from its spherical shape (FigureS3D). The diameter of the nucleus for a spread cell depends on the physical properties of the cell, and can be used as a crosschecking point for the validity of selected nucleus parameters. The nuclear area of A375M2 melanoma cells allowed to spread on collagen surfaces in vitro, were measured for the control state, for Y27632 treated cells with reduced myosin II driven contractility and for Dasatinib treated cells with increased myosin II driven contractility. The average nuclei diameters are calculated for the equivalent circular areas. The values obtained from experiments give a mean nucleus diameter of $11.67 \pm 2.11\ \mu m$, $13.10 \pm 1.47\ \mu m$, and $10.30 \pm 0.70\ \mu m$ for control, Y27632 treated and Dasatinib treated, respectively. Equivalent computational experiment results are $10.94 \pm 0.56\ \mu m$, $11.79 \pm 0.59\ \mu m$, and $10.12 \pm 0.27\ \mu m$ (FigureS3E).

Blebs

A bleb is initiated at an agent when the forces acting on the agent due to internal pressure of the cell exceed the cortex-membrane linker forces, in accordance with current levels of PIP_2, c_{LNK} (see Proteins - *PIP_2 fluctuations and Inverse Transform Sampling*). When a bleb is initiated, there is residual cortex at the bleb rim, which initially is devoid of myosin II [2, 9, 10]. During the expansion phase, the blebs are filled mainly with the cytosol, lacking larger organelles, and a structured cytoskeleton[2]. Once a bleb is initiated at an agent, the agent's linkers and drag coefficient with the

cell interior are set to represent its new behaviour ($f_{COR} = f_{COR}^{bleb}$, c_{MYO}=0). With successive delays, Δt_{COR} and Δt_{MYO}, actin (FigureS1D-E) and myosin accumulates in the bleb [9, 11], increasing f_{COR} and c_{MYO} respectively (*Cortex Reassembly in Blebs*). The cortex remaining at the bleb neck is represented as a separate layer, which decays over time [2, 12, 13]. During the expansion phase blebs can tear the membrane off the cortex, facilitating further growth of the bleb neck and bleb body (see *Bleb Necks*). The bleb may form adhesions with the ECM only when the actin levels reach those at regular cell surface levels.

Cortex Reassembly in Blebs

During simulation, the cortex fraction inside a given bleb is updated with a function fitted to the experimental data (FigureS1D-E, Equation S17). t_{BLEB} is the time from the onset of bleb retraction. The parameters of the function are, a=2.5, b =1.3, and c=-0.26. f_{COR} is the actin fraction of the cortex, and f_{COR}^{BLEB} is the cortex fraction residual at the bleb rim at the onset of bleb initiation, and the cortex fraction is calculated according to

$$f_{COR} = f_{COR}^{BLEB} + \left(1 - f_{COR}^{BLEB}\right)\frac{g\left(t_{BLEB}\right) - g\left(0\right)}{g\left(\infty\right) - g\left(0\right)} \quad ,with \qquad \text{S17}$$

$$g\left(t\right) = \frac{a}{b + \exp\left(c \times t\right)} \ .$$

Bleb Necks

Upon bleb initiation, it is necessary to model the cortex at the neck of the expanding bleb as a separate layer. In the simple definition of bleb necks, the double layer of the bleb neck is represented as a new linker between the borders of the bleb. Both actin and myosin levels at the linker are equal to the myosin level at the given section of the cortex before bleb initiation. During the expansion phase, the membrane and residual cortex of the bleb will pull the membrane at the borders of the bleb. Depending on the linker protein levels at the border, together with the internal pressure, these forces can facilitate further tearing of the membrane from the cortex. The amount of actin and ideal length of springs are recorded as the bleb is torn on the sides. The neck linker is initiated with 1 pseudo-node, and the number of nodes is increased accordingly as the bleb tears on its sides. Keeping track of the number of nodes used in forming the bleb neck is necessary to carry on discrete calculations of forces acting on the borders of the bleb. Forces acting on an agent at the bleb neck are:

$$\mathbf{F}_{\mathbf{NECK}} = F_{NECK}\hat{\mathbf{l}}_{NECK} \ , \qquad \text{S18}$$

$$F_{NECK} = k_{COR}^{NECK}\left(\frac{L_{NECK}}{n_{pn}+1} - L_{pn}^{0}\right) - \eta_{COR}^{NECK}\ \hat{\mathbf{l}}_{NECK}.\left(\frac{\mathbf{v}-\mathbf{v}_{\mathbf{NECK}}}{n_{pn}+1}\right) + k_{MYO}^{NECK}\frac{L_{NECK}}{n_{pn}+1} \ .$$

In the above equation, the first term is the elastic response of the cortex, the second term is the viscous response of the cortex and the third term is the effect of myosin contractility. $\mathbf{v}_{\mathbf{NECK}}$ and $\hat{\mathbf{l}}_{NECK}$ are, respectively, the velocity of, and the unit vector in the direction of, the border on the other side of the bleb. n_{pn} is the number of nodes at the bleb neck, and L_{pn}^{0} is the ideal length of the linkers between the nodes of the bleb neck (FigureS2F). The cortex remaining at the bleb neck decays over time [2, 12, 13], the spring constant and viscous resistance of the cortex, and myosin spring constant are reduced accordingly (Equation S19-21). The decay time τ_{NECK} is selected to be 40 s, in line with actin renewal rate. Superscript 0 indicates the value at the onset of bleb initiation. The equations used for the updates are

$$k_{COR}^{NECK}\left(t+dt\right) = k_{COR}^{NECK}\left(t\right) - \frac{k_{COR}^{0,NECK}}{\tau_{NECK}}dt \ , \qquad \text{S19}$$

$$\eta_{COR}^{NECK}\left(t+dt\right) = \eta_{COR}^{NECK}\left(t\right) - \frac{\eta_{COR}^{0,NECK}}{\tau_{NECK}}dt \ , \qquad \text{S20}$$

$$k_{MYO}^{NECK}\left(t+dt\right) = k_{MYO}^{NECK}\left(t\right) - \frac{k_{MYO}^{0,NECK}}{\tau_{NECK}}dt \ . \qquad \text{S21}$$

In the improved definition of the bleb necks, the cortex is explicitly modelled, similar to the rest of the cell F-actin cortex. Instead of the pseudo nodes of the simple definition, upon initiation of the bleb, the first bleb neck node is positioned at the point of the cell surface agent that detached from the cortex to form the bleb. At each tearing event, a new bleb neck node is added to the bleb neck, at the position of the torn agent. The elastic forces and viscous damping are calculated in the same manner as the rest of the cell surface. The protein levels are regulated in the same manner of simple bleb necks. The benefit of this explicit modelling is that curving and local position changes of the bleb neck can be represented. This in turn, allows us to investigate the interactions of the bleb neck cortex with the cell nucleus.

Actin Polymerisation Based Protrusions

Initiation of actin polymerisation based protrusions is probabilistic, and inversely proportional to myosin concentrations. At the tip of the protrusions, the membrane is pushed out by the polymerising actin [14], with a force $\mathbf{F}_{\mathbf{TIP}}$ of 10 pN [15, 16]. Myosin from the cytosol diffuses into the newly polymerised regions of the protrusion (see *Actin*

Cortex and Myosin). The protrusions are filled with an actin mesh, and the model takes this into account through our definition of linkers between the sides of the protrusion (Figure1A). Similar to bleb necks, these linkers decay, as the protrusion ages. Protrusions may spread on the ECM, and compared to a free protrusion, a spreading protrusion is less likely to stop elongating. A protrusion may adhere to the ECM during its complete lifecycle; with the exception of the protrusion tip, which cannot adhere during elongation phase.

The occurrence rate of protrusion initiation is,

$$P^0 = 1 - \exp\left(-k_f^0 dt\right), \qquad \text{S22}$$
$$P = P^0 \exp\left(-b_{PROT}\left(c_{MYO} - c_{MYO}^0\right)\right).$$

k_f^0 is the normal formation rate per agent, c_{MYO} is the myosin concentration at the agent, c_{MYO}^0 is the normalised myosin concentration, 1. The formation rate is fitted to the experimental data, 4 x 10^{-4} s^{-1} (Table S1). The probability is shifted depending on the myosin concentration, with parameter b_{PROT}, fitted to experimental data (FigureS2D). Protrusions cannot form on blebs. Each protrusion is initiated with a random protrusion angle and, as long as the protrusion is not spreading on a surface, the tip force is applied in the direction of initiation. Theoretical estimations and measurements are in the range 3-20 pN for filopodia and up to 20 pN for lammelipodia [15, 16]. In his work, we used a value of 10 pN.

To ensure balance of internal forces, during the elongation phase of the protrusion, the counterbalancing force of the tip force is distributed evenly to the regions neighbouring the protrusion tip. As long as the elongation rate at the tip is below the protrusion elongation rates reported for filopodia and lammelipodia[17-19], the actin springs' ideal lengths are elongated to the springs' current lengths, such that there is no strain due to elongation. This threshold is selected as 0.2 μm s^{-1}.

The protrusion stops elongating at time, dt_{PROT}, of 5-10 s if it is not spreading on a surface. The value is selected to give protrusion lengths of the non-spreading protrusions in the ranges reported in the literature, 1-2 μm [16]. Once a protrusion hits a surface with a suitable angle, less than 85 degrees, it starts spreading on the surface; the elongation direction is updated to follow the surface of the filament. A spreading protrusion can stop elongating on a surface for a variety of reasons, such as accumulated myosin, or the cell moving in the opposite direction and pulling the protrusion back. The retraction phase is simply defined as the halt of active polymerisation at the protrusion tip, and by the rules defining the polymerisation (see top of this section). The actin mesh inside the protrusion is represented as a set of

linkers. For each of the agents on the sides of the protrusion, the closest point on the other side of the protrusion is calculated. The linker spring has the ideal length of 0.2 μm, representing the thickness of the protrusion[16]. The linkers decay with time, the strength of the linker spring is determined by the age of the current agent of interest, and the point linked on the other side.

Proteins

Within the linkers, actin is renewed, with the actin renewal time of τ_{COR}, bringing the ideal lengths of cortex springs closer to their current lengths. Myosin levels in agents are regulated by myosin diffusion dynamics with the cytosol; the equilibrium myosin level depends on the overall contractility level of the cell and the influence of the imposed polarity. Using the inverse transform sampling method[20], on experimentally generated PIP_2 concentration distributions, the local cortex membrane linker protein levels, c_{LNK}, are allowed to stochastically fluctuate within each agent (FigureS1H, *Proteins - PIP_2 fluctuations and Inverse Transform Sampling*).

During the simulation, to keep the equal distance spacing of the initial discretisation, agents are added and deleted from the cell; myosin concentration, PIP_2 levels and actin spring ideal lengths are redistributed accordingly.

Proteins - Actin Cortex and Myosin

Equilibrium myosin depends on the given polarity profile of the cell and the position of the agent on the cell surface. The value in each agent is updated with diffusion to/from cell interior, depending on the equilibrium myosin level (Equation S23), and the actin renewal brings the ideal length of the spring to the current length via equation S24:

$$c_{MYO}\left(t+dt\right) = c_{MYO}\left(t\right) + D_{MYO}\left(c^{eq}_{MYO}\left(t\right) - c_{MYO}\left(t\right)\right)dt \ , \qquad \text{S23}$$

$$L^0_i\left(t+dt\right) = L^0_i\left(t\right) + \frac{L_i\left(t\right) - L^0_i\left(t\right)}{\tau_{COR}}dt \ . \qquad \text{S24}$$

Proteins - PIP_2 Fluctuations and Inverse Transform Sampling

The experimental measurement of PIP_2 fluctuations is given in FigureS1H. This cumulative distribution is obtained by measuring the intensities on non-blebbing cell surfaces from a number of images like FigureS1F. The background intensity is then subtracted from the measurements to account for time dependent bleaching of the fluorescent protein, and the values are initially normalised with the membrane marker channel (FigureS1G). Finally, the whole data set is normalised to the mean,

and this normalised data is used to generate the cumulative distribution function sampled in stochastic fluctuations (FigureS1H).

The normalised PIP_2 distribution is best fitted to a gamma distribution with shape parameter k=3.98 and scale parameter $\theta = 0.24$, and the cumulative distribution function is calculated accordingly. Each agent on the cell surface is initiated with a linker protein concentration randomly selected from this normalised distribution. The mean of PIP_2 concentration $\left\langle c_{LNK}^0 \right\rangle$, is chosen such that the mean adhesion protein, per agent at the resting state is equal to 1. This gives $\left\langle c_{LNK}^0 \right\rangle$= 25 ($L^0$=0.2 μm, w_{model}=0.2 μm). During the update of linker proteins, the probability of the current linker concentration is calculated. Then a random step size in the range ±2.5% is selected, and the probability is updated with the selected step size. The new concentration, corresponding to the new probability, is assigned as the linker concentration of the agent. The strength of adhesion between the cortex and the membrane, for any given length of cell surface, is then obtained from the following equation where L is the total length associated with the region, $\left\langle c_{LNK} \right\rangle$ is the average linker protein concentration of the region, and F_{LNK}^0 is the force per unit linker protein concentration:

$$F_{LNK} = \left\langle c_{LNK} \right\rangle L w_{\text{model}} F_{LNK}^0 \quad . \qquad \text{S25}$$

Cell - ECM Interactions

The model cell has no slip binding to ECM filaments, i.e. while an agent is adhered to a filament surface, it has zero velocity for simulations with rigid ECM, and it moves only with the velocity of the deformation of the ECM surface in simulations with flexible ECM. Binding events are treated as reversible, with cell–ECM binding modelled using the well established Bell Model [21]. The Bell model of cell-cell and cell-substrate adhesion is a simple yet successful representation of the complex adhesion phenomena. It have been used in modelling adhesion phenomena such as cell membrane-cell cortex adhesion, generic cell – ECM adhesion, leucocyte – tumour cell interactions involving integrin β2, clustering of integrins, integrin-cortex and integrin-ECM interactions of lammelipodia [22-26].

In the model, formation of bonds is dependent on distance and spontaneous formation rate, k_{on}. Adhesion rupture is dependent on the ratio of forces applied to concentration of adhesion protein, and on the spontaneous off rate (Equations S26-S28). Adhesion strengths corresponding to variable protein levels were assessed with two methods. First, using adhesion force data available for focal contacts, the

range of adhesion units for an agent of the model that would fit with realistic focal complex strengths is determined. Second, computations are performed which mimic atomic force microscopy experiments aimed at measuring the whole cell–ECM adhesion force. (FigureS2G-H, *Adhesion Mapping and Atomic Force Microscopy Simulations*). Penetration of the cell into the ECM filaments is prevented by a hard-wall potential.

In the Bell model, the probability of bond formation is given as:

$$P_{on} = \begin{cases} 1-\exp\left(-k_{on}dt\right) & if \quad \text{distance} < r_{cut}^{ad} \\ 0 & if \quad \text{distance} > r_{cut}^{ad} \end{cases} . \qquad \text{S26}$$

And adhesion breakage probability as:

$$P_{off} = 1-\exp\left(-k_{off}dt\right) \text{ ,where} \qquad \text{S27}$$

$$k_{off} = k_{off}^{0}\exp\left(\frac{r_0 F}{N_{ad}k_b T}\right) \qquad \text{S28}$$

Here, k^0_{off} is the instantaneous dissociation rate, F is the force acting on the agent (excluding the component in the direction of the adhered surface); N_{ad} is the units of adhesion protein at the agent; r_0 is the distance defining the well of the energy potential; k_b is Boltzman constant; and T is temperature. Detachment of one unit of protein will lead to increased force on the remaining adhesions, causing catastrophic detachment [27]. Following this argument, during simulation, if one unit of adhesion protein detaches within the agent, the agent will cease to be adhered to the surface.

A hard wall potential is used to prevent the cell from penetrating into ECM filaments. The reaction force a filament can apply to the pushing cell surface cannot be higher than the force applied by the cell. Hence, the applied force is capped, proportional to the forces driving the agent towards the filament. For the stability of the simulation, the cap is selected slightly higher than the total forces. The magnitude of the force (pN), in which the direction is normal to the filament surface at the point of approach, is given by

$$F_{HW} = \begin{cases} 0 & if \quad d > r_{cut}^{HW} \\ a_{HW} \dfrac{r_{cut}^{HW} - d}{d^{b_{HW}}} & if \quad d < r_{cut}^{HW} \text{ and } a_{HW} \dfrac{r_{cut}^{HW} - d}{d^{b_{HW}}} < F^{CAP} \\ F^{CAP} & if \quad d < r_{cut}^{HW} \text{ and } a_{HW} \dfrac{r_{cut}^{HW} - d}{d^{b_{HW}}} > F^{CAP} \end{cases}, \qquad \text{S29}$$

where r_{cut}^{HW} is the cut off distance above which no force is applied (selected as 0.1) μm. d is the distance between the filament and the agent. a_{HW} is $10^{-2}\, pN\mu m^{(1-b_{HW})}$ and b_{HW} is 0.5. The values are set to prevent the cell from penetrating into the filaments, while not preventing it from adhering to the filament.

Adhesion Mapping and Atomic Force Microscopy Simulations

The strength of focal complexes has been measured to be 1−3nNμm^{-2} [28]. The average area per cell surface agent, calculated from model width and the average length associated with an agent is 0.04μm^2. Therefore, for adhesion strength equivalent to a focal complex, the forces necessary to detach an adhered agent from its substrate should be within the range 0.04−0.12nN. Adhesion maturation to focal complexes takes approximately 60s, a period that is not included in the model. If a 60s period is allowed for adhesion and another 60s for possible detachment, the force per adhesion unit protein within an agent resulting in a 90 per cent probability that the agent will detach within 120s, $(F/Nb)^{Pull\ f=0.90}$, can be calculated. Fitting this force term to the range 0.04−0.12nN, the adhesion protein units per agent, defining a cell forming focal contacts with its substrate under control conditions should be in the range 7−21 adhesion units. Here, it is important to note that the level of adhesion does not necessarily correspond to the number of proteins in a given agent.

This scaling gives a rough estimate of the adhesion level for the cell with unperturbed cell–ECM adhesion. However, considering the stochastic nature of binding and detachment events, and the multiple cell surface agents involved in adhering the model cell to ECM filaments, a further mapping of the adhesion units to the forces necessary to detach cells from the ECM is required. To calculate the adhesion strengths for different levels of adhesion proteins, we simulated atomic force microscopy experiments (FigureS2H-I). The cell is simulated to spread on the surface and then pushed towards the surface with, 1 nN force, for 50 seconds. The pushing force is released, and the cell is allowed to rest for another 50 seconds. At the end of this period, the cell is pulled away from the surface for 200 seconds, and it is recorded if the cell is still adhered to the surface or torn off at the end of the pulling

period. With the known total pulling force and initial adhered area of the cell, force per μm^2 is calculated. The state of adhesion at the end of the experiment, as a function of adhesion protein level and applied force is obtained, providing a benchmark of the model to real adhesion values. The forces applied detach the cross-section of the cell in the model, with the defined width w_{MODEL}. A rough scaling from the 2D model to 3D suggests ~70 fold increase in the force. The adhesion level 10 would start failing at 84 nN, which is within the ranges reported in the literature: MDCK cells 20 nN, keratocytes 45 nN and fibroblasts 2000 nN [29, 30].

Experimental Data Fitting

Parameters that are not available in the literature, and could not be estimated by calculation, are fitted to experimental measurements of bleb sizes, bleb dynamics, protrusion frequency, and protrusion dynamics (Table S2).

For maximum bleb size, maximum bleb expansion velocity and maximum retraction velocity measurements, for both experimental and computational experiments, cumulative distribution functions are prepared. Bin sizes for generating the cumulative distributions are selected as 0.0025μm for maximum bleb size, and 0.005 $\mu m s^{-1}$ for bleb expansion and retraction rates. The total sum of squares and residual sum of squares are calculated from each bin point value of the cumulative distribution function obtained from the computational experiment, and each bin point value of the cumulative distribution function of the experimental data. Then the R^2 fit between experimental data, and data from each of the parameter sets from the computational experiments are calculated[31]. The parameter set with the highest R^2 score for the average of all three cumulative distributions (size, expansion and retraction velocities), is selected as the fitted model parameter set. For the parameter set utilised in the model, the fit score is 0.948.

Using light microscopy (LM), the maximum bleb sizes from time-lapse videos could be measured (Figure2B). For the computational experiments, all membrane detachment areas can be measured, even those too small to be detected experimentally from light microscopy imaging. To confirm the existence of small blebs, scanning electron microscopy (SEM) images of blebbing cells under the same experimental conditions are taken (FigureS1A-C). Following the confirmation of small blebs in real cells, bleb dynamics data generated by the model for only blebs of sufficient size are included in comparison with the experimental measurements. The threshold of size is selected as the minimum bleb size that could be measured in light microscopy experiments, which is 0.51μm. Similarly, for the comparison of bleb size distribution from random snapshots of the model with SEM data, a size threshold of 0.067 μm is used. The bleb sizes for LM, SEM, model (maximum), and model (snapshot) are in the range: $1.1 \pm 0.40 \mu m$, $0.4 \pm 0.25 \mu m$, $0.89 \pm 0.41 \mu m$, and $0.25 \pm 0.30 \mu m$ respectively (Figure2B, FigureS1A-C). Cross-sections of control cells,

myosin inhibited cells and serum stimulated cells, were interpreted to determine the numbers of spreading protrusions. The number of protrusions was then used to fit the protrusion initiation rate as a function of myosin levels (FigureS2C-D).

Calculated Parameters

Tinevez *et al* reports the effective cortex elastic modulus $E_c h$ as 0.00024 μN μm^{-1}, where h is the thickness of the cortex. The relation between the reported value and the spring constants in our 2D model can be given as

$$F_{ACT} = E_{ACT} \frac{\Delta l}{l^0} \left(h \; w_{cell} \right) \; and \qquad \text{S30}$$

$$k_{COR} = \frac{E_{ACT} \left(h \; w_{cell} \right)}{\left\langle l^0 \right\rangle} \; . \qquad \text{S31}$$

where $\left\langle l^0 \right\rangle$ is the average ideal spring length of the agents in the system. Then with the discretisation of the system at 0.2 μm intervals and model width of 0.2 μm, the cortex spring constant is obtained as 0.00024 μNμm^{-1}. The ratio of viscous to elastic resistance of cortex is selected as 25 s, from the range reported in Coskun *et al*, 2007, giving η_{COR} as 0.006 μN s μm^{-1}. The bulk modulus of the cell is calculated as 2250 Pa from the reported cytoplasmic elasticity $E_{CYT} / 1 - 2\nu_{CYT}$ 6750 Pa [10], with the relation

$$K_{CELL} = \frac{1}{3} \frac{E_{CYT}}{1 - 2\nu_{CYT}} \; . \qquad \text{S32}$$

Internal pressure for HeLa cells is reported in the range 17-110 Pa [2]. Using the Laplace Law, with a cell of 8.5 μm diameter, and the total cortex tension reported in Tinevez *et al*, the internal pressure of the cell is in the range 95 Pa. Considering the midpoint reported by Charras *et al*, and Tinevez *et al*, we obtain an estimate of 79.25 Pa for intracellular pressure. For simplicity, we select our ideal pressure as 80 Pa. With known K_{CELL}, the myosin spring constant is calculated to give the selected pressure of 80 Pa under the steady state condition. As an initial estimate for internal viscosity of the cell we ran simulations mimicking the experiments of Lam *et al* [32], resulting in the range 8x10^{-5}-2x10^{-4}μN s μm^{-2}. Starting our trials within this range, we fitted η_{CELL} to our experimental data to obtain 1x10^{-4}μN s μm^{-2}.

Minimiser

An over-damped modelling approach does not implicitly conserve the momentum of the system. Since a key interest is to understand cell motility with low to zero adhesion to the ECM, the model is required to strictly reproduce the phenomenon that a cell should not be able to drift. Therefore, inspired by Buenemann *et al* [33], a minimisation step is imposed upon the calculations. It should be pointed out that this approach will not be able to model situations where the cells can "swim" in a viscous fluid, and our model is restricted to situations where the cells generate traction relying on extracellular matrix or a synthetic equivalent.

In a friction free environment, due to conservation of momentum, as the cell changes its shape, its centre of mass should stay at the same point, moving the whole cell backwards if the cell protrudes some part of its body forwards, and vice versa. On the other hand, under any form of anchoring to the environment; the cell should be able to translocate its body. The minimiser takes into account the cell centre of mass displacement from the previous step, adhesion to, and clashing with, the filaments. The energy penalties are selected such that clashing with the filaments or disrupting the position of an adhered agent implies significantly higher penalty than displacement of centre of mass. As a result, the minimiser keeps the cell centre of mass at the same point, unless there is anchoring to the environment; and does not interfere with displacement of the cell under any other condition. To minimise its energy, the cell can translocate its centre of mass and rotate. The cell is treated as a rigid body during minimisation. The equations defining the energy space searched by minimiser are:

$$E_{TOT} = E_{DISP} + E_{AD} + E_{CLASH}, \text{ where} \qquad \text{S33}$$

$$E_{DISP} = e_1\left(\partial_{CM}^2 + \partial\theta\right), \qquad \text{S34}$$

$$E_{AD} = \sum_i \delta_{AD}^i \frac{e_2 c_{AD}^i}{1+\exp\left(-12\partial_{AD}^i\right)} - \frac{e_2 c_{AD}^i}{2}, \text{ with} \qquad \text{S35}$$

$\delta_{AD}^i = 1$ if agent is adhering, 0 otherwise ,

$$E_{CLASH} = \sum_i \delta_{CLASH}^i e_3 \partial_{CLASH}^2, \text{ with} \qquad \text{S36}$$

$\delta_{CLASH}^i = 1$ if agent penetrates into filament, 0 otherwise .

∂_{CM} is the displacement of the cell centre of mass from its position in the previous step, $\partial\theta$ is the rotation of cell body in radians. Summations for adhesion and clash

energies are over all agents. c^i_{AD} is the concentration of adhesion proteins in the agent, and ∂^i_{AD} is the displacement of the agent from its adhesion point. The functions shape is selected to have zero contribution to energy when agent is at its adhesion point (∂^i_{AD}=0). ∂^i_{CLASH} is the distance the agent penetrated into the filament. With the above explained constraints, the value of e_1 is set to 10^{-5}; e_2 to 2; and e_3 to 10^{-5}.

Limitaitons of the Model

The high speed of blebbing strategies in discontinuous environments might suggest that bleb-driven migration would be greatly favoured during evolution; however it is clear that polymerisation-driven protrusions are widely used. Our model highlights a limitation of blebbing based migration; as blebs become larger the bleb neck can hinder the motion of the nucleus. This observation is supported by high resolution intravital imaging. In addition, there are other reasons why protrusions may be favoured that are not accounted for in our model. Many of the critical environments for cell migration in normal physiology may be continuous surfaces, either confined or non-confined. In these geometries, protrusion based strategies have similar velocities to blebbing strategies. Polymerisation-driven protrusions may have greater fidelity at following directional cues. The continuous tearing of the plasma membrane from the actin cortex that is inherent in blebbing migration is likely to disrupt the formation of signalling complexes that may sense and respond to tactic cues. For example, we find that recycling endosomes, which are critical for efficient signal transduction by many receptors, are unable to enter blebs (data not shown). Finally, we do not calculate the energy consumption required for the different types of migration. Furthermore, cancer cell invasion occurs in many matrix geometries that we have not considered, is frequently dependent on matrix degradation and/or interactions with other cell types. Within amoeboid blebbing motility itself, our experimental analysis shows multi-layered blebs, where new blebs are formed on top of retracting blebs, progressively leaving behind layers of decaying bleb neck cortex. Ultimately, the role of these variables will need to be integrated with a more sophisticated understanding of the feedback mechanisms that function between the ECM and cell, such as the strengthening of cell-ECM adhesions with applied contractile forces, or down-regulation of contractile machinery at adhesion sites in longer time scales [34, 35]. Our model provides a basis for further theoretical consideration of the impact of these factors on cell migration.

Computation

The model is written in C++. The system is solved by the 4th order Runge-Kutta (RK) method. The matrix itself in each step of RK is solved by using the Intel MKL libraries Pardiso solver [36]. The minimization is done via GNU scientific library's random n-

simplex minimiser [37]. The visual interface for the simulation toolbox is constructed in OpenGL. The Intel compiler is used with parallelization option for compiling the package. Depending on the intracellular and environment conditions, a simulation equivalent to 20 minutes takes 6-12 hours on an 8-processor Intel computer.

Supplementary References

1. Raucher, D. & Sheetz, M.P. Characteristics of a membrane reservoir buffering membrane tension. *Biophysical journal* **77**, 1992-2002 (1999).
2. Charras, G., Coughlin, M., Mitchinson, T. & Mahadevan, L. Life and Times of a Cellular bleb. *Biophysical Journal* **94**, 1836-1853 (2008).
3. Boal, D. *Mechanics of the Cell*. (Cambridge University Press, 2001).
4. Herant, M. & Dembo, M. Cytopede: a three-dimensional tool for modeling cell motility on a flat surface. *Journal of computational biology : a journal of computational molecular cell biology* **17**, 1639-1677 (2010).
5. Hochmuth, R.M., Ting-Beall, H.P., Beaty, B.B., Needham, D. & Tran-Son-Tay, R. Viscosity of passive human neutrophils undergoing small deformations. *Biophysical journal* **64**, 1596-1601 (1993).
6. Wolf, K. & Friedl, P. Mapping proteolytic cancer cell-extracellular matrix interfaces. *Clinical & experimental metastasis* **26**, 289-298 (2009).
7. Guilak, F., Tedrow, J. & Burgkart, R. Viscoelastic properties of the cell nucleus. *Biochemical and Biophysical Research Communications* **269**, 781-786 (2000).
8. Caille, N., Thoumine, O., Tardy, Y. & Meister, J.-J. Contribution of the nucleus to the mechanical properties of endothelial cells. *Journal of biomechanics* **35**, 177-187 (2002).
9. Charras, G., Hu, C.-K., Coughlin, M. & Mitchison, T. Reassembly of Contractile Actin Cortex in Cell Blebs. *J Cell Biol* **175**, 477-490 (2006).
10. Tinevez, J.-Y. *et al.* Role of cortical tension in bleb growth. *Proceedings of the National Academy of Sciences* **106**, 18581-18586 (2009).
11. Cunningham, C.C. Actin polymerization and intracellular solvent flow in cell surface blebbing. *The Journal of cell biology* **129**, 1589-1599 (1995).
12. Kardash, E. *et al.* A role for Rho GTPases and cell-cell adhesion in single-cell motility in vivo. *Nat Cell Biol* **12**, 47-53; sup pp 41-11 (2009).
13. Maugis, B. *et al.* Dynamic instability of the intracellular pressure drives bleb-based motility. *J Cell Sci* **123**, 3884-3892.
14. Alberts, B. *et al. Molecular Biology of the Cell*. (Garland Science, 2002).
15. Cojoc, D. *et al.* Properties of the force exerted by filopodia and lamellipodia and the involvement of cytoskeletal components. *PloS one* **2** (2007).
16. Mogilner, A. & Rubinstein, B. The Physics of Filopodial Protrusion. *Biophys J* **89**, 782-795 (2005).
17. Raucher, D. & Sheetz, M.P. Cell spreading and lamellipodial extension rate is regulated by membrane tension. *The Journal of cell biology* **148**, 127-136 (2000).
18. Raucher, D. *et al.* Phosphatidylinositol 4,5-bisphosphate functions as a second messenger that regulates cytoskeleton-plasma membrane adhesion. *Cell* **100**, 221-228 (2000).
19. Mallavarapu, A. & Mitchison, T. Regulated actin cytoskeleton assembly at filopodium tips controls their extension and retraction. *The Journal of cell biology* **146**, 1097-1106 (1999).
20. grouptheory Mathematical Tools or Statistics, Monte Carlo, Group Theory. *Physics Letters B* **667**, 316-339 (2008).

21. Bell, G.I. Models for the specific adhesion of cells to cells. *Science* **200**, 618-627 (1978).
22. Brugues, J. *et al.* Dynamical organization of the cytoskeletal cortex probed by micropipette aspiration. *Proceedings of the National Academy of Sciences* **107**, 15415-15420 (2010).
23. Schreiber, C., Stewart, M. & Duke, T. Simulation of cell motility that reproduces the force-velocity relationship. *Proceedings of the National Academy of Sciences of the United States of America* **107**, 9141-9146 (2010).
24. Liang, S. *et al.* Two-dimensional kinetics of β2-integrin and ICAM-1 bindings between neutrophils and melanoma cells in a shear flow. *American Journal of Physiology - Cell Physiology* **294**, C743-C753 (2008).
25. Paszek, M., Boettiger, D., Weaver, V. & Hammer, D. Integrin Clustering Is Driven by Mechanical Resistance from the Glycocalyx and the Substrate. *PLoS Comput Biol* **5**, e1000604 (2009).
26. Macdonald, A., Horwitz, R. & Lauffenburger, D. Kinetic model for lamellipodal actin-integrin 'clutch' dynamics. *Cell adhesion & migration* **2**, 95-105 (2008).
27. Seifert, U. Rupture of Multiple Parallel Molecular Bonds under Dynamic Loading. *Physical Review Letters* **84**, 2750-2753 (2000).
28. Choquet, D., Felsenfeld, D.P. & Sheetz, M.P. Extracellular matrix rigidity causes strengthening of integrin-cytoskeleton linkages. *Cell* **88**, 39-48 (1997).
29. Moore, S., Roca-Cusachs, P. & Sheetz, M. Stretchy Proteins on Stretchy Substrates: The Important Elements of Integrin-Mediated Rigidity Sensing. *Developmental Cell* **19**, 194-206 (2010).
30. Friedrichs, J., Manninen, A., Muller, D. & Helenius, J. Galectin-3 regulates integrin alpha2beta1-mediated adhesion to collagen-I and -IV. *The Journal of biological chemistry* **283**, 32264-32272 (2008).
31. Miller, I. & Miller, M. *John E. Freund's Mathematical Statistics with Applications (7th Edition)*. (Prentice Hall, 2003).
32. Lam, J., Herant, M., Dembo, M. & Heinrich, V. Baseline mechanical characterization of J774 macrophages. *Biophysical journal* **96**, 248-254 (2009).
33. Buenemann, M., Levine, H., Rappel, W.-J. & Sander, L. The role of cell contraction and adhesion in dictyostelium motility. *Biophysical journal* **99**, 50-58 (2010).
34. Parsons, T., Horwitz, A. & Schwartz, M. Cell adhesion: integrating cytoskeletal dynamics and cellular tension. *Nature Reviews Molecular Cell Biology* **11**, 633-643 (2010).
35. Tzima, E., del Pozo, M., Shattil, S., Chien, S. & Schwartz, M. Activation of integrins in endothelial cells by fluid shear stress mediates Rho-dependent cytoskeletal alignment. *The EMBO Journal* **20**, 4639-4647 (2001).
36. Schenk, O. & Gärtner, K. Solving unsymmetric sparse systems of linear equations with PARDISO. *Future Generation Computer Systems* **20**, 475-487 (2004).
37. Press, W., Flannery, B., Teukolsky, S. & Vetterling, W. *Numerical Recipes in C: The Art of Scientific Computing, Second Edition*. (Cambridge University Press, 1992).